A distinct element method numerical investigation of compaction processes in highly porous cemented granular materials

G. Dattola[1], C. di Prisco[2], I. Redaelli[2] and S. Utili[3,*,†]

[1]Department of Civil, Energetical, Environmental and Material Engineering, Università "Mediterranea" di Reggio Calabria, Reggio Calabria, Italy
[2]Department of Civil and Environmental Engineering, Politecnico di Milano, Milan, Italy
[3]School of Engineering, University of Warwick, U.K. formerly at University of Oxford, U.K.

1. INTRODUCTION

Natural porous rocks are quite common in many regions of the world, especially in Italy, where these materials have been used in the past for the construction of buildings and monuments. We refer for
instance to calcarenite [1] and tuffs (de' Gennaro *et al.*, 2000), in which the porosity often reaches
values larger than 0.6 [2]. Analogously, in nature it is not rare to find pumice stones with porosities as large as 0.73 and conchyliates with porosities of around 0.65 [3]. Up to now, the mechanical response of these materials has been mainly studied both experimentally and numerically (Nova *et al.*, 2003) by
taking into account their shear strength; in contrast, in some engineering problems like, for instance, the design of deep foundations of structures placed on underground cavities (piles/micropiles) the study of
compaction banding is quite crucial. An original study of this topic, via small scale experimental tests
on shallow foundations, is Nova and Parma [4].

In the last decades, very porous artificial conglomerates are also becoming rather common in the geotechnical practise: they are used for instance in special engineering applications in tunnelling and obtained as by-products of waste soil treatment. As was reported by Cucino *et al.* [5], very porous artificial conglomerates are employed in the construction of tunnels within swelling rocks to reduce

*Correspondence to: S. Utili, School of Engineering, University of Warwick, U.K. formerly at University of Oxford, U.K.

†E-mail: s.utili@warwick.ac.uk

the actions on the tunnel lining. Moreover, very porous artificial materials are often the result of the cementation of soils and waste materials [6], which are engineered to improve their physical/ chemical properties using a large variety of binding agents (lime, cement, fly ash, etc.). Jarofix, for instance, characterised by a porosity of about 70%, is obtained by mixing sodium jarosite with Portland cement and lime [7]. Cement admixed clays are very common cemented soils, by-products of ground improvement measures undertaken by cement stabilisation. The porosities of these materials are very high, with values of void ratio up to 5 [8, 9] and the presence of a bimodal pore structure with large spherical macro-voids along with inter-particle voids [10, 11]. The compaction processes within these natural/artificial materials are frequently characterised by the onset of compaction bands: Arroyo *et al.* [7] observed them in Jarofix and artificial conchyliades and Castellanza *et al.*[3] in Gasbeton.

This paper aims to investigate compaction processes taking place within very porous rocks either natural or artificial where a large decrease in void ratio is associated with the failure of bonds binding grains rather than grain crushing, which instead is observed at very large confining pressures on rocks characterised by lower porosities [12–21].

Arroyo *et al.* [7] and Castellanza *et al.* [3] observed that under oedometric conditions in both highly porous cemented soils and soft rocks like calcarenites: (i) compaction bands can take place at low vertical pressures (4–10 MPa); (ii) the mechanical response is markedly affected by the presence of large voids within the porous matrix; and (iii) damage mainly takes place in the bonds, these latter ones being weakness points in the microstructure. For all these reasons, the authors have decided to numerically analyse the compaction phenomenon by starting from a simplified description of the microstructure and by employing a numerical strategy based on the distinct element method (DEM) capable of taking into account the microstructure of this type of materials. Until now, few authors have employed DEM to investigate compaction processes in cemented porous materials. Katsman *et al.* [22] conducted numerical simulations on an ideal two-dimensional porous material made up of a regular network of linear springs without modelling each rock/soil grain individually. Wang *et al.* [23] ran more realistic two-dimensional DEM analyses, but 2D analyses imply that the real porosity and the 3D kinematics of the motion of grains cannot be replicated. In the authors' opinion, this is a fundamental limitation on the study of compaction bands because both porosity of the material and kinematics of the motion of the soil grains play a crucial role. Finally, more recently, Marketos and Bolton [24] investigated the occurrence of compaction bands triggered by grain crushing via 3D DEM analyses.

Hereafter, an idealised highly porous geomaterial, made of bonded spherical grains, rather than a specific geomaterial, is considered. No quantitative agreement between numerical results and available experimental data is thus expected. The numerical results that will be illustrated in this paper highlight how the microstructural variables govern the mechanical response of the system. For instance, it will be shown that, when compaction bands occur, the internal length of the material is mainly related to the size of the macro-voids, whereas, when shear bands take place, the characteristic length is mainly related to the grain size distribution [25, 26]. Moreover, it will be shown that the fragility/ductility of the mechanical behaviour of bonds, together with the material porosity, rules the occurrence of localization at the macro-level.

2. NUMERICAL PROCEDURE

In very porous soft rocks, the presence of macro-voids and bonds can be observed in images obtained via optical microscope (Figure 1(a)) and by scanning electron microscope images (Figure 1(b)), [27]. As is shown in Ciantia and Hueckel [27], soft rocks like calcarenites can be thus interpreted as double porosity materials. The macropores severely affect the mechanical response of the material because, under compression, the destructuration of the material is mainly governed by their collapse. For these reasons, the idealised material conceived by the authors will be thus characterised by the following: (i) presence of macro-voids; (ii) a high void ratio; and (iii) rigid grains bonded to one another.
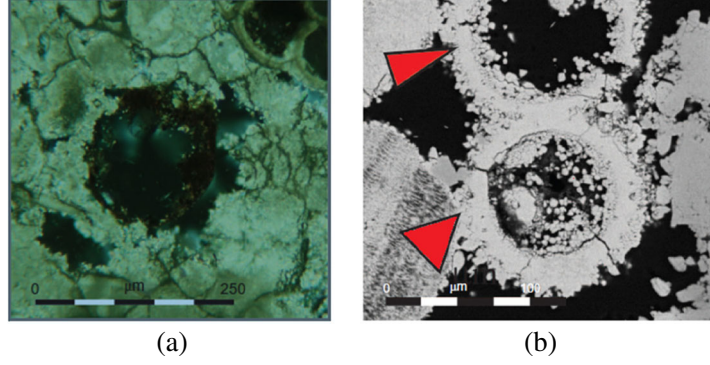
(a)   (b)

Figure 1. (a) Macropores in calcarenite observed via polarised light microscope. (b) Macropores in calcarenite observed via scanning electron microscope (SEM). The arrows indicate the presence of bonds [27].

2.1. Sample generation

The numerical campaign consisted of 16 oedometric tests on cylindrical specimens. In all the simulations, gravity was absent because geostatic stresses were assumed to be negligible in comparison with the applied axial stress. The initial height H_0 and diameter Δ of specimens were determined after assigning the following: (i) the initial porosity n (the majority of the samples being characterised by an initial porosity equal to 0.7); (ii) the total number of grains N_p (this was kept approximately constant and equal to $16\,000$ for all the generated specimens (Table II)); (iii) the grain size distribution; and (iv) the specimen slenderness, $\alpha = H_0/\Delta$, which was kept constant and equal to 2.

For a cylindrical specimen, V_t, the total specimen volume is related to the cylinder diameter as

$$V_t = \frac{H_0 \pi \Delta^2}{4} = \frac{\pi \alpha \Delta^3}{4} \tag{1}$$

Moreover,

$$V_t = \frac{V_s}{1 - n} \tag{2}$$

with V_s being the volume of the solid fraction. From Eqns (1) and (2), the size of the sample diameter was calculated as

$$\Delta = \sqrt[3]{\frac{4V_s}{(1 - n)\alpha\pi}} \tag{3}$$

with the volume of the solid fraction, V_s , calculated as:

$$V_s = \sum_{i=1}^{N_p} \frac{4}{3}\pi \left(\frac{\phi_{pi}}{2}\right)^3 \tag{4}$$

where ϕ_{pi} is the diameter of the i-th grain.

An additional goal of the procedure has been the generation of a specimen with a set of macro-voids homogeneously distributed in space to generate specimens with both large void ratios and non-negligible coordination number. The main geometrical parameters of the introduced microstructure are as follows: (i) the ratio of macro-void size over the average grain size; and (ii) the number of macro-voids per unit volume.

To obtain a random distribution of pseudo-spherical macro-voids within the specimen, the following numerical procedure was employed:

- Initially, two different groups of particles were generated within the cylinder: (i) 'micro-particles' with linearly varying diameters and (ii) 'macro-particles' with a constant diameter ϕ_m.
- The method employed to generate the samples is the so-called radius expansion method [28]. This technique allows for the generation of a spatially random grain size distribution with a homogeneous network of contacts and low lock-in forces (so that specimens with negligible initial self-stresses are generated). In order to investigate the influence on the material mechanical response of the macro-voids size, simulations were run for two sizes of the macro-void diameter: $\phi_1 = 2.5\,mm$ and $\phi_2 = 6.13\,mm$. On the other hand, the final distribution of the micro-particle (grain) size diameters adopted is the same in all the tests. This is a uniform distribution with the grain diameter ranging from $\phi_{p,\min} = 0.98\,mm$ to $\phi_{p,\max} = 1.47\,mm$.
- After generation, (Figure 2), the macro-particles are deleted to attain the desired macro-voids and bonds are assigned to all the pairs of particles in contact. Bonds were simulated in PFC3D by employing the so-called 'parallel bonds': beam elements with circular cross section, whose constitutive law is described in the following. The adopted parallel bond was assigned a radius, $\overline{R}$, of 0.7 times the minimum radius of the two grains in contact. Given the adopted particle size distribution, the area of the parallel bonds ranged from $A_{\min} = 0.37\,mm^2$ to $A_{\max} = 0.83\,mm^2$.

The number of macro-particles/macro-voids was determined by trial and error. Specimens with different numbers of macro-voids and the same overall porosity were generated. The authors observed that when the number of macro-voids was above a threshold value, stresses were present at the end of the generation procedure (i.e. the end of particle radii expansion); whereas when the number of macro-voids was below the threshold, no stresses were present. Because the overall porosity is fixed (e.g. $n = 0.7$), the lower the number of macro-voids is, the lower the number of contacts among particles is and consequently the number of bonds. In order to generate a sample free from lock-in forces but at the same time with a complete network of bonded particles, that is without any unbonded particles being present, the sample with the largest possible number of macro-particles but with negligible stresses on the boundaries at the end of the generation procedure (i.e. less than $1\,kPa$) was adopted. In Table II, both the obtained standard coordination numbers, c_N^{pb}, defined as the number of contact per particle, and the mechanical coordination number [29], C_N^{pb}, which excludes floating particles and rattlers (particles with only one contact), are reported. Although the values of coordination number are quite small, nevertheless, the obtained microstructure is mechanically stable because of the presence of bonds holding particles together.

2.2. Contact laws and micromechanical parameters

In DEM, the simplest contact law, governing the mechanical interaction between two unbonded particles, is a linear spring together with a divider along the normal direction and a linear spring together with a
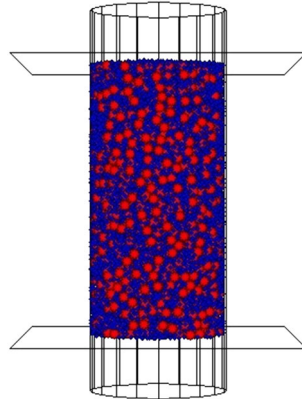

Figure 2. Cylindrical sample after the generation procedure, with micro-particles (rock/soil grains) in blue and macro-particles (to become macro-voids) in red.

frictional slider along the tangential direction. The contact stiffness is defined by both the normal and shear stiffness of the two contacting entities (either particle or wall). The values of the particle normal and shear stiffnesses (k_n^p, k_s^p) and the intergranular friction coefficient (μ^p) employed are reported in Table I. These are typical values selected in DEM simulations for granular materials when the linear contact law is employed [30–32]. Top and bottom platens and lateral walls were set to be frictionless and much stiffer than the particles (Table I). The grain density ρ_p was set equal to $2650 kg/m^3$.

To simulate the action of cementitious bonds, two different bond models, herein called standard parallel bond (SPB) model and damage parallel bond (DPB) model, respectively, were employed and are described in the following sections. The SPB model was obtained by activating at the same time two bond models already available in PFC3D [33]: the so-called 'contact' and 'parallel' bond models. The 'contact bond' between two particles prevents tangential irrecoverable slippage whilst the 'parallel bond' transmits both elastic forces and moments between the two bonded particles. The DPB model instead was implemented by the authors in the code via an ad-hoc routine.

Two different regularising damping approaches are commonly employed in DEM analyses: the so-called local damping and viscous damping. The former type of damping consists of increasing decelerations and decreasing accelerations of particles of a fixed fraction, δ, [34]. In the latter case instead, two dashpots, one along the normal direction, ruled by parameter β_n, and the other one along the tangential direction, ruled by parameter β_s, are added to the contact model, so that a damping force opposing the relative particle motion and proportional to the relative particle velocities is active. The dimensionless parameters β_n and β_s represent the ratio between the applied damping and the critical damping coefficients.

Calibration of physically meaningful values of damping is very difficult because the current lack of experimental measurements on the dissipative phenomena taking place at the microscopic level (e.g. asperity shearing off, grain fracturing, etc.). For this reason, it is desirable to introduce a damage model (DPB) able to directly control the fragility/ductility of the bonds. Herein in the following, both approaches are employed and critically discussed.

2.2.1. Standard parallel bond model. In this model, bonds behave elastically until brittle failure occurs. The default PFC3D 'parallel bond' is defined as a function of two stiffness coefficients and of the ratio of the bond radius over the minimum grain radius of the bonded particles. The parallel bond can be interpreted as a set of elastic springs uniformly distributed over a circular cross section. The normal and shear 'distributed' stiffnesses were taken as $\overline{k}^n = 5 \times 10^{12}$ Pa/m and $\overline{k}^s = 2.5 \times 10^{12}$ Pa/m. These parameters were selected according to Marketos and Bolton [24] and Potyondy and Cundall [28]. Failure takes place when either the maximum tensile stress exceeds the normal bond strength (σ_c) or the maximum shear stress exceeds the bond shear strength (τ_c) (Table II). At failure, the entire elastic energy stored in the bond is released instantaneously. The maximum tensile and shear stresses acting on the parallel bond periphery can be calculated via beam theory.

2.2.2. Damage parallel bond model. For the reasons previously mentioned, the authors have chosen to implement a damage rheological model dealing with a set of generalised stress–strain variables.

A similar approach has been proposed by Potyondy [35] to investigate damage occurring at bond level due to stress-corrosion reactions. Differently from that approach, in which the damage reduces the diameter of bonds, here the damage process is simulated as a progressive reduction in the mechanical properties of bonds.

In the DPB model conceived by the authors the process leading to the breakage of bonds is gradual. Bond failure is assumed to occur at the end of a progressive reduction in the mechanical properties (stiffness and strength) of the bond. The adopted DPB model is herein illustrated by employing generalised variables in terms of forces, **Q**, and displacements, **q**, defined as it follows:

Table I. Micromechanical parameters of particles and walls.

k_n^p [N/m]	k_s^p [N/m]	μ^p	k_n^w [N/m]	k_s^w [N/m]	μ^w
4×10^6	2×10^6	0.5	4×10^8	2×10^8	0

Table II. Parameters used for the simulations with elasto-brittle and elasto-damage contact model.

Test	N_p	N_m	ϕ_m [mm]	κ	c_N^{pb}	C_N^{pb}	$\beta^n=\beta^s$	δ	ω	$\overline{\sigma}_c$ [Mpa]	$\overline{\tau}_c$ [Mpa]	σ_0 [Mpa]	τ_0 [Mpa]	$\dot{v}$ [Hz]
SPBl07κ2_1	16492	2244	2.5	2	2.35	3.18	0.0	0.3	—	130	130	—	—	0.76
SPBl07κ2_2	16492	2244	2.5	2	2.35	3.18	0.0	0.7	—	130	130	—	—	0.76
SPBl07κ2_3	16492	2244	2.5	2	2.35	3.18	0.0	0.9	—	130	130	—	—	0.76
SPBv07κ2_1	16492	2244	2.5	2	2.35	3.18	0.0	0.0	—	130	130	—	—	0.76
SPBv07κ2_2	16492	2244	2.5	2	2.35	3.18	0.3	0.0	—	130	130	—	—	0.76
SPBv07κ2_3	16492	2244	2.5	2	2.35	3.18	0.6	0.0	—	130	130	—	—	0.76
SPBv07κ2_4	16492	2244	2.5	2	2.35	3.18	0.3	0.0	—	130	130	—	—	0.61
SPBv07κ2_5	16492	2244	2.5	2	2.35	3.18	0.3	0.0	—	130	130	—	—	0.38
SPBv07κ2_6	16492	2244	2.5	2	2.35	3.18	0.3	0.0	—	130	130	—	—	0.19
DPB07κ2_1	16492	2244	2.5	2	2.35	3.18	0.0	0.0	0.8	—	—	250	250	2.75
DPB07κ2_2	16492	2244	2.5	2	2.35	3.18	0.0	0.0	0.6	—	—	250	250	2.75
DPB07κ2_3	16492	2244	2.5	2	2.35	3.18	0.0	0.0	0.4	—	—	250	250	2.75
DPB07κ5_1	16491	181	6.13	5	2.34	3.41	0.0	0.0	0.6	—	—	250	250	2.75
DPB05κ2_1	16490	520	2.50	2	4.61	4.79	0.0	0.0	0.6	—	—	250	250	2.75
DPB05κ2_2	16490	520	2.50	2	4.61	4.79	0.0	0.0	0.8	—	—	250	250	2.75

$$Q = \begin{bmatrix} N \\ V \\ M \\ M_t \end{bmatrix} \tag{5}$$

with $N = \overline{F}^n \cdot \mathbf{n}$, $V = \overline{F}^s \cdot \mathbf{s}$, $M = \overline{M}^s \cdot \mathbf{r}$ and $M_t = \overline{M}^n \cdot \mathbf{n}$. $\overline{F}^n$ and $\overline{F}^s$ represent the axial and the shear force acting on the parallel bond, respectively, and $\overline{M}^n$ and $\overline{M}^s$ the torque and bending moments. $\mathbf{s}$ is a unit shear vector, and $\mathbf{r}$ a unit moment vector parallel to the shear force and the bending moment, respectively. The corresponding displacements and rotations can be grouped in a vector, $\mathbf{q}$:

$$q = \begin{bmatrix} U^n \\ U^s \\ \theta^s \\ \theta^n \end{bmatrix} \tag{6}$$

with $U^s = \mathbf{U}^s \cdot \mathbf{r}$ and $\theta^s = \boldsymbol{\theta}^s \cdot \mathbf{r}$. U^n and θ^n represent the axial relative displacement and rotation, respectively, between two bonded particles, whilst U^s and θ^s, the tangential relative displacement and rotation.

The adopted elasto-damage model is based on the following assumptions: (i) damage occurs isotropically; and (ii) no irreversible displacements and rotations take place, that is, the elastic stiffness during unloading is lower than the stiffness exhibited during the first loading. Because of the first hypothesis, the amount of damage is expressed by means of only a scalar state variable, D, ranging from 0, for intact bonds, to 1, for fully damaged bonds. With the progression of damage, D increases according to a prescribed damage law. The constitutive relationship introduced in the following is formulated in the framework of standard damage models [36]. According to the so-called equivalence principle,

$$\widetilde{\mathbf{Q}} = \mathbf{D}^e \mathbf{q} \tag{7}$$

where $\widetilde{\mathbf{Q}}$ is the associated effective force vector and $\mathbf{D}^e$ is the elastic stiffness matrix. $\widetilde{\mathbf{Q}}$ is defined as

$$\tilde{\mathbf{Q}} = \frac{\mathbf{Q}}{1 - D} \tag{8}$$

The elastic stiffness $\mathbf{D}^e$ has the following form:

$$\mathbf{D}^e = \begin{bmatrix} \bar{k}^n A & 0 & 0 & 0 \\ 0 & \bar{k}^s A & 0 & 0 \\ 0 & 0 & \bar{k}^n I & 0 \\ 0 & 0 & 0 & \bar{k}^s J \end{bmatrix} \tag{9}$$

with A, I and J being the area, moment and polar moment of inertia of the parallel bond cross section, respectively. From Eqns (7) and (8), the vector of the generalised forces can be obtained

$$\mathbf{Q} = (1 - D)\mathbf{D}^e\mathbf{q} \tag{10}$$

This equation defines the constitutive relationship in terms of generalised variables once the evolution law of the damage variable D is assigned. The activation of damage is ruled by a threshold function defined in the space of the generalised load variables (N, V, M and M_t):

$$g = g(\mathbf{Q}, \chi(D)) \tag{11}$$

where $\chi(D)$ is the vector of internal variables. The threshold function is analogous to the yield function in classical plasticity theory: if $g < 0$, the material behaves elastically and $\dot{D} = 0$ so that χ is constant, whereas for $g = \dot{g} = 0$, damage occurs, $\dot{D} > 0$, so that χ reduces and as a consequence the threshold surface ($g = 0$) shrinks omothetically.

For the sake of simplicity, the influence of torque on the threshold function was neglected; hence, the activation of damage process is exclusively governed by N, V and M. The threshold function adopted is a modification of the mathematical expression first proposed by Neal [37]:

$$g(\mathbf{Q}, \chi(D)) = \left| \frac{M}{\overline{M}} \right|^{\xi_1} + \left(\frac{N}{\overline{N}} \right)^2 + \frac{\left(\frac{V}{\overline{V}} \right)^4}{1 - \left(\frac{N}{\overline{N}} \right)^2} - 1 \tag{12}$$

where the vector of the internal variables, χ, is defined as follows:

$$\chi = \begin{bmatrix} \overline{N} \\ \overline{V} \\ \overline{M} \end{bmatrix} \tag{13}$$

with $\overline{N}$, $\overline{V}$ and $\overline{M}$ are the coordinates in the space of the generalised forces of the intersection points between the current threshold surface and the coordinate axes (N, V and M), respectively. The shape of the threshold surface is shown in Figure 3.

Because the Newton–Raphson algorithm adopted to compute the damage model equations (Appendix) requires differentiability of the threshold function in all the points of its domain, an extra parameter, ξ_1, was added to the original Neal's formulation to make it differentiable. When $\xi_1 = 1$, the original Neal's expression is obtained. If a value of ξ_1 just slightly larger than 1 is chosen (for instance $\xi_1 = 1.001$), differentiability of the function is ensured, and the difference between the original shape of the Neal's threshold surface and the one here adopted is practically negligible.
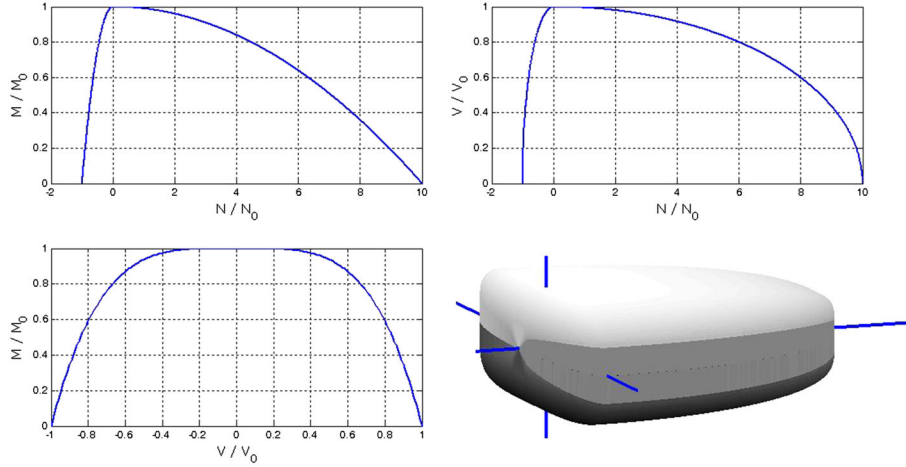
Figure 3. The adopted threshold surface (Eqn (12)) in the N-V-M space.

The evolution of the internal variable vector χ was assumed as follows:

$$\chi = \begin{bmatrix} \overline{N} \\ \overline{V} \\ \overline{M} \end{bmatrix} = \begin{bmatrix} \widetilde{N_0} \\ V_0 \\ M_0 \end{bmatrix} (1-D)^\omega \qquad \text{with } \omega < 1 \qquad (14)$$

with

$$\widetilde{N_0} = \begin{cases} N_0 & \text{for } N < 0 \\ \xi_2 N_0 & \text{for } N \geq 0 \end{cases} \qquad (15)$$

with $\xi_2 > 1$. ω is a parameter governing the ductility of the mechanical response, that is, the rate of shrinkage of the threshold surface. The larger ω is, the higher is the rate of damage (Appendix). Because the damage parameter D reaches 1 only asymptotically, we assumed that bond breakage occurs at $D = 0.99$, with bonds being deleted as soon as $D = 0.99$. Note that unlike the original surface proposed by Neal, our threshold surface is non-symmetrical, because of the introduced parameter ξ_2 representing the ratio of purely compressive strength over purely tensile strength (Figure 3). Here, a compressive strength 10 times the tensile one was assumed so that $\xi_2 = 10$.

Analogously to the elasto-brittle bond model, the onset of damage is related to the maximum normal stress σ_0 and the maximum tangential stress τ_0 of the bond:

$$\begin{aligned} N_0 &= \sigma_0 A = \sigma_0 \cdot \pi \cdot \overline{R}^2 \\ V_0 &= \tau_0 A = \tau_0 \cdot \pi \cdot \overline{R}^2 \\ M_0 &= \sigma_0 \frac{I}{\overline{R}} = \frac{1}{4}\sigma_0 \cdot \pi \cdot \overline{R}^3 \end{aligned} \qquad (16)$$

where $\overline{R}$, A and I are the radius, the area and the moment of inertia of the parallel bond, respectively.

In the Appendix, the detailed implementation of the elasto-damage bond model into the code is illustrated. In summary, the DPB model is a function of five parameters (σ_0, τ_0, ξ_2, ω and $\overline{R}$), the first three are related to the bond strength, ω to the bond ductility and $\overline{R}$ to the bond geometry. The key feature of the bond model here introduced is that the parameters employed are clearly related to either the geometry or the material properties of the bond.

2.3. Determination of the representative elementary volume

The results of any either numerical or experimental test are reliable if and only if the tested specimens are big enough to be representative of the material analysed, nevertheless, in many publications on DEM, the question whether the adopted volume is a representative elementary volume (REV) is only rarely tackled (e.g. see [38]). For the material here investigated, the size of the REV is a function of the following: (1) the size of particles; (2) the size of macro-voids; and (3) the average distance among macro-voids, which was calculated as the average distance between the centres of two adjacent macro-voids minus the macro-void radius.

To identify a suitable REV, we considered the mechanical response of specimens before any breakage of bonds (no localisation has yet occurred) until their mechanical response is linear elastic. The specimens were loaded by moving the top platen downwards with the bottom platen fixed. In the initial loading phase, the global stiffness of the specimens can be conveniently expressed in terms of the oedometric Young modulus, E_{oed}, defined as the ratio between the axial stress σ_a, calculated as the axial force acting on the upper platen over the platen area and the nominal axial strain, as the vertical displacement Δz of the upper platen over H_0.

Both particle size distribution and initial porosity of specimens were kept unchanged in the majority of the simulations so that the REV size depends exclusively on the size of the macro-voids. As is evident from Figure 4, by increasing the specimen size, the variation in E_{oed} becomes progressively smaller until a horizontal asymptote is reached, implying that in case of $\kappa = 2$ (Figure 4(a)), specimens with $H_0/\phi_{p,mean} > 45.2$, corresponding to $N_p > 10\,000$ can be taken as a REV and, analogously (Figure 4(b)), specimens with $\kappa = 5$ and average distance between macro-voids equal to $4mm$ turn out to be representative for the material.

2.4. Detection of compaction bands

Compaction banding is a localization process causing the loss of uniformity in both the strain and stress fields within the specimens. Compaction bands are commonly classified as tabular zones of pure compressive deformation aligned orthogonally to the direction of the maximum compressive stress. To detect the formation of compaction bands, the authors employed two different strategies. The first is based on detecting broken and damaged bonds (see Figures 15, 16, 18, 10, 21, 22 and 26). According to this approach, the development of zones of higher concentration of damage signals the presence of compaction bands. This is the default approach to capture the onset of compaction bands in experimental tests (Olsson and Holcomb [17] and Baud *et al.* [21]). However, the presence of zones of higher concentration of bond breakages is not sufficient to prove the development of a compaction band. To this end, a second strategy, based on the analysis of the strain field, was employed. This requires the calculation of a reliable local measure of strains, which is a particularly challenging problem in case of discrete element simulations. To evaluate the field of vertical strain,
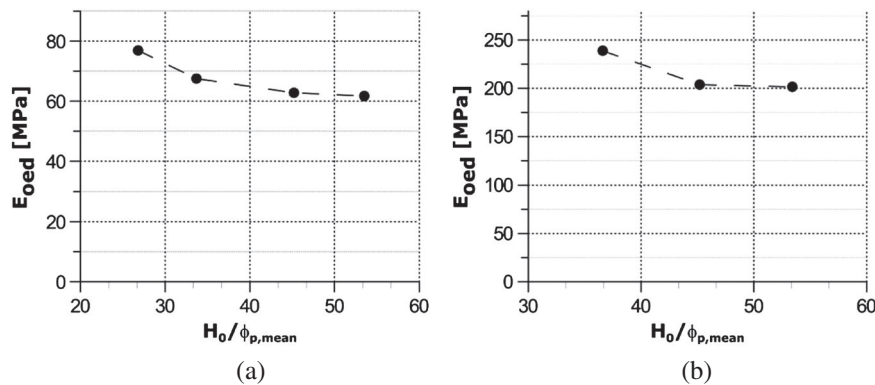

Figure 4. Oedometric Young elastic modulus, E_{oed}, versus sample height, H_0, normalised by the mean particle size, $\phi_{p,mean}$, for samples with different number of macro-voids: (a) $\kappa = 2$ and (b) $\kappa = 5$.

two techniques were adopted: the first one being based on mesh-free interpolants and the second one on a simplified method to measure the variation of void ratio within the sample [39].

In recent years, several kinematic homogenization techniques have been proposed in the literature to calculate strains in particulate media. All these techniques rely on the calculation of average displacement gradients from the displacements and rotations of single particles. O'Sullivan *et al.* [40] showed that mesh-free interpolants are particularly effective in detecting strain localisation. They employed the so-called moving least square reproducing kernel (MLSRK) interpolant, first proposed by Liu *et al.* [41] which was employed in this paper, too. This method requires the selection of a value for the so-called dilation parameter, ρ, that represents the size of the window function, which is a mathematical function used as interpolant for the displacement field achieved from the displacements recorded for the particles.

The second technique is based on the subdivision of the sample into a number of equal size layers [42]. At each step, the subdivision is repeated. The number of layers is kept constant with each layer being of the same size. The void ratio of each layer, e_L, was calculated from the total volume of the layer and the volume of solids, V_{sL}. The average volumetric strain ε_{volL}, that is, the average vertical strain ε_{zL} per layer, is calculated as follows:

$$\varepsilon_{zL} = \varepsilon_{volL} = \frac{\Delta V_{vL}}{V_{0L}} = \frac{\Delta e_L \cdot V_{s0L}}{V_{0L}} \tag{17}$$

with Δe_L the variation of void ratio in the layer, V_{0L} the initial volume of the L-th layer and V_{s0L} the initial volume of solids belonging to the L-th layer.

3. RESULTS

Numerical tests were performed by employing both SPB and DPB models. In Table II, a summary of the values of the parameters employed is provided. Each test is denoted by the acronym 'xPB$yz\kappa w\_i$' where x indicates the type of bond model: S for SPB and D for DPB; y indicates the type of damping employed: l for local and v for viscous; z indicates the initial porosity of the specimen; w represents the value of the parameter κ; and i represents the identification number of the test.

All the specimens were loaded by moving downwards the upper platen with the bottom platen kept fixed. The imposed nominal axial strain rate $\dot{v}$ is reported in Table II. The difference between the force acting on the upper platen and the reaction force on the lower platen was constantly monitored and resulted to be negligible throughout all the tests (Figure 5). As long as no localization due to the collapse of macro-voids occurs, the specimen continues to be homogeneous; therefore, if the granular assembly is considered as a continuum body, the presence of equal reaction forces at the boundaries
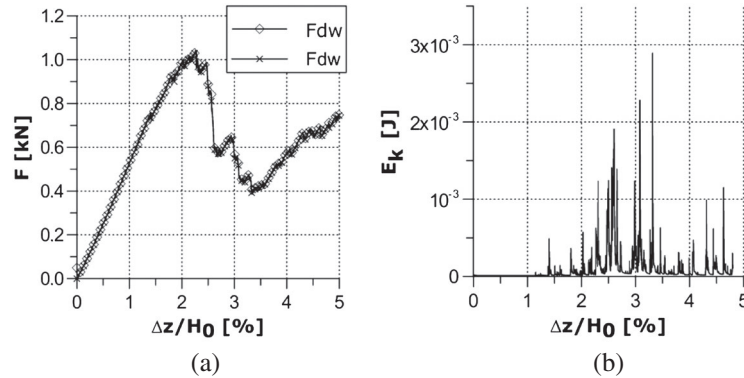

Figure 5. Graphs relative to test SPBl07κ2_2. During the test, the lower plate is fixed, whereas the upper plate moves downwards. (a) Forces acting on the upper F_{up} and lower F_{dw} platen against the nominal axial strain. (b) Total Kinetic energy E_k of the granular system against the nominal axial strain.

implies a uniform stress state. Now, according to the equilibrium equations of continuum mechanics (conservation of linear momentum), inertial body forces are equal to the gradient of the stress tensor, which is nil in this case because no body forces are present (gravity is absent) and no pressure differential is applied on the boundaries (equal reaction forces from the platens); hence, it can be concluded that the specimen is under quasi-static conditions, that is, the inertial forces present are very small in comparison with the static forces. Note that had both platens been moving (e.g. bottom platen moving upwards and upper platen moving downwards), the presence of equal reaction forces would not imply the uniformity of the stress field in the specimen because a symmetrical stress gradient could develop with the line of symmetry located at half the sample height. Once localization occurs because of the collapse of macro-voids, quasi-static conditions are no longer in place even if the reaction forces on the platens remain equal (Figure 5(a)) so that spikes of kinetic energy arise in the specimen due to the accelerations experienced by the particles involved in the collapse of macro-voids (Figure 5(b)). The occurrence of localization implies that the sample is no longer homogeneous so that the aforementioned considerations on quasi-staticity of the sample are no longer valid and the stress field inside the region(s) where compaction band(s) develop may be different from the field in the rest of the sample.

In Figure 6 the stress–strain curves of several tests for the same specimen size ($H_0 = 6.54$ cm, $\Delta = 3.27$ cm) but for different bond models and damping types are plotted: it emerges that the mechanical response of the system is significantly affected by both the constitutive model of the bonds and the type of damping adopted. In the following sections, the influence of each factor on the mechanical response of the system is investigated.

3.1. Influence of the damping law (SPB model)

The mechanical response of the tested specimen was investigated for various values of δ for local damping ($\delta = 0.0$; $\delta = 0.3$; $\delta = 0.7$; $\delta = 0.9$) and of β^n, β^s for viscous damping ($\beta^n = \beta^s = 0.0$; $\beta^n = \beta^s = 0.3$; $\beta^n = \beta^s = 0.6$) with the obtained stress–strain curves plotted in Figure 7. From the graphs in the figure, two stages of the test can be identified: the first one being the part where the trend is linear and the second one the part where it is nonlinear. In the first stage, the specimen exhibits a linear elastic behaviour and deforms under quasi-static conditions, and all the curves coincide because of the fact that under quasi-static conditions damping does not affect the mechanical response of the material [43]. In
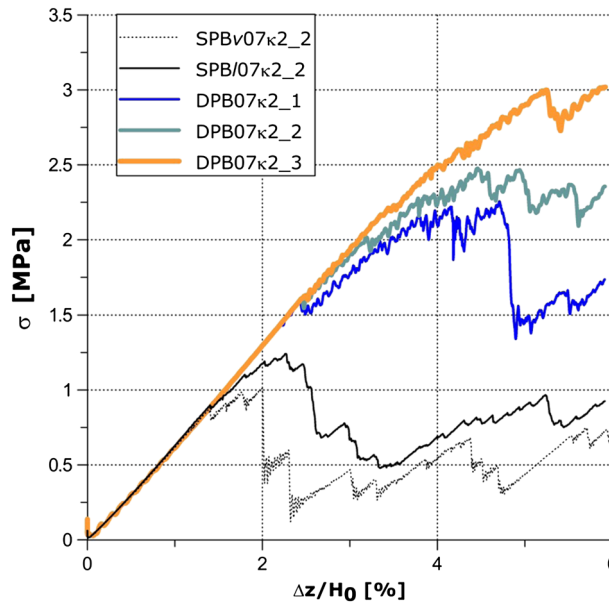

Figure 6. Comparison between the $\sigma_a - \Delta z/H_0$ curves obtained in different tests with different values of parameters (Table II).
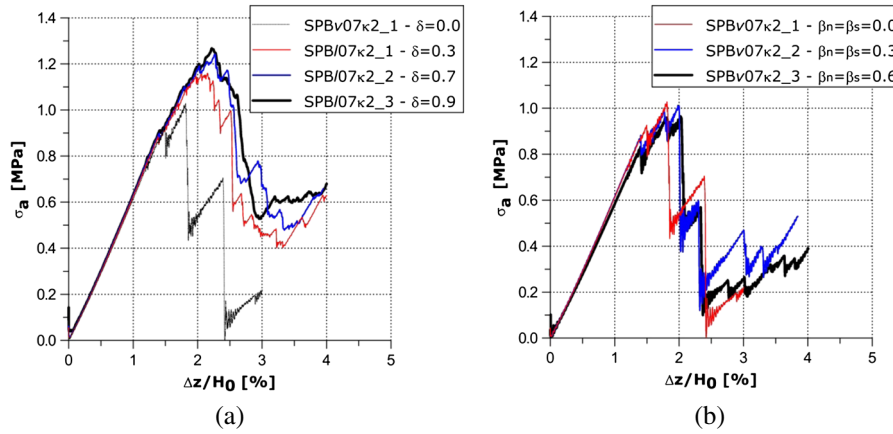
Figure 7. Comparison between the $\sigma_a - \Delta z/H_0$ curves obtained for different values of (a) the local damping coefficient δ and of (b) the critical damping ratios $\beta s = \beta n$.

the second phase instead, specimens experience inertial forces due to the movement of particles let free by the failures of the bonds binding them. It emerges that the local damping is significantly more effective in reducing the material fragility than the viscous damping.

Moreover, it can be observed that the peak of the axial stress is highly affected by the value adopted for the local damping (Figure 7(a)) in contrast with the negligible influence exerted by the viscous damping (Figure 7(b)). The observed trend can be explained considering that when the stress peak is reached, collapse of several macro-voids has taken place allowing the previously bonded particles freedom of movement. Now local damping acts directly on particle accelerations reducing them, whereas the viscous damping acts only when particles come into contact, therefore unlike the viscous damping, local damping is effective at reducing the speed of the collapse of the macro-voids, which in turn affects the dynamic equilibrium established in the specimen and therefore the stress peak.

In Figure 8, the dependence of the mechanical response on the loading rate applied is illustrated for tests run with viscous damping of $\beta^n = \beta^s = 0.3$. Because all the curves coincide during the initial elastic phase, it
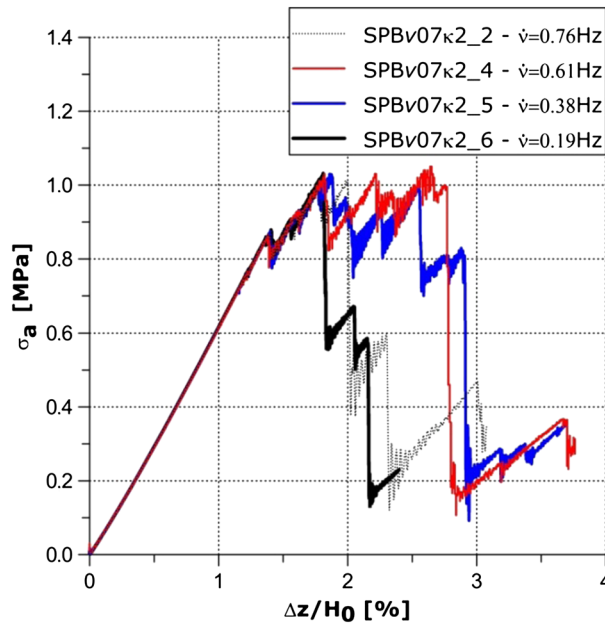

Figure 8. Comparison between the $\sigma_a - \Delta z/H_0$ curves obtained for different values of the nominal axial strain rate v.

can be concluded that the loading rate does not affect the mechanical response of the specimens as long as they remain homogeneous. Also, the values of peak stress, reached after localization has taken place, are the same. The only noticeable difference in the plotted stress–strain curves is about the value of axial displacement ($\Delta z/H_0$) when a significant stress drop occurs. This value is not correlated by any trend (e.g. proportionality) with the loading rate applied but appears to be random.

3.2. Detection of compaction band propagation

The overall mechanical response of test SPBl07κ2_2 (local damping on; $n=0.7$; $\kappa=2$) is hereafter illustrated (Figure 9). The average radial stress, σ_r, was calculated as the ratio between the sum of the normal contact forces acting on the lateral surface of the cylinder and its lateral area. In the first part of the axial stress – nominal axial strain curve (Figure 9(a)), the response is linear elastic until approximately $\Delta z/H_0 = 1.3\%$ with all the bonds being intact. After this stage, a marked deviation from the linear trend is observed with a few broken bonds uniformly distributed in the specimen (Figure 9(b)). At $\Delta z/H_0 = 2.3\%$, the peak of the axial stress (point B in Figure 9(a)) is achieved. Subsequently, a steep drop in stress takes place up to point C (Figure 9(a)). At this point, a large number of broken bonds are present in the middle of the sample, in a band perpendicular to the vertical direction of compression (Figure 9(d)). Looking at the plot of the number of bonds along the z-coordinate (Figure 9(e)), a high concentration of broken bonds is evident: the majority of breakages occurring in a thick band (about 1/4 of the initial height of the sample, 6 times the diameter of the macro-voids) with only a tiny amount of breakages outside the band.
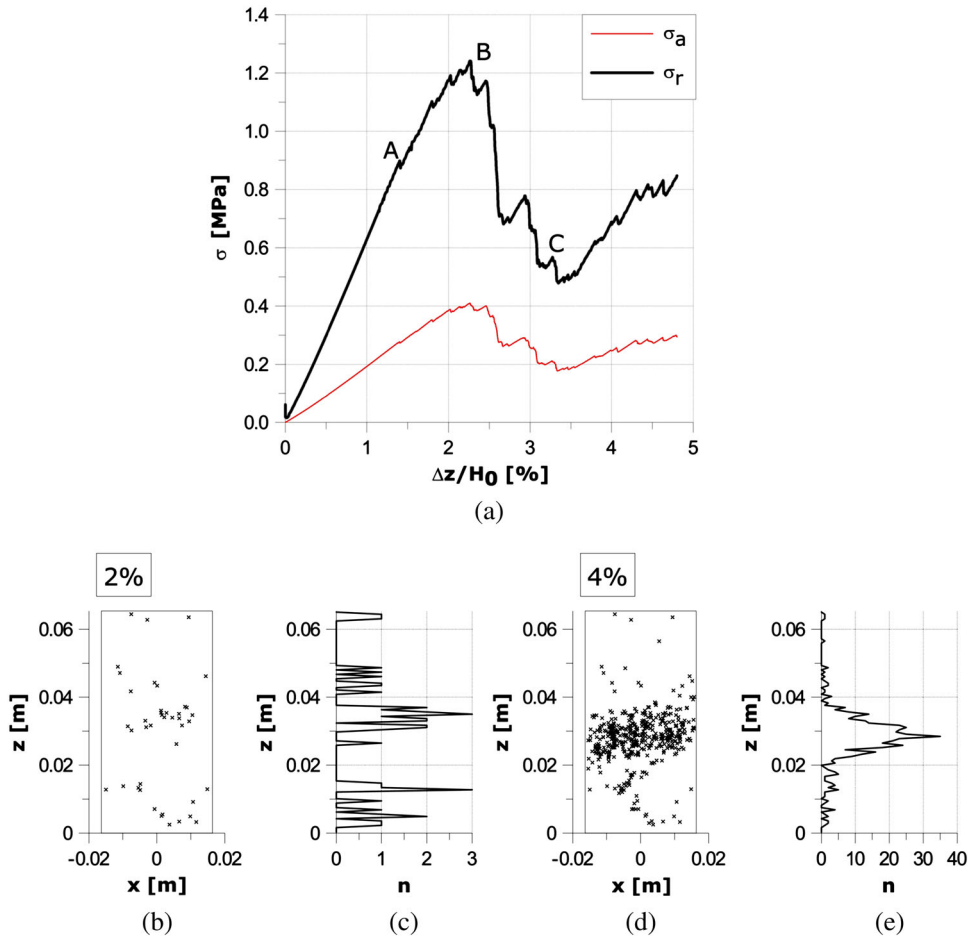

(a)

| (b) | (c) | (d) | (e) |

Figure 9. Test SPBl07κ2_2: (a) $\sigma_a - \Delta z/H_0$ and $\sigma_r - \Delta z/H_0$; (b) and (d) spatial distribution of the broken bonds in the vertical plane (x is the horizontal axis whilst z is the vertical one) at $\Delta z/H_0 = 2\%$ and $\Delta z/H_0 = 4\%$, respectively; (c) and (e) number of broken bonds along the vertical axis.

In Figure 10, the strain field within the sample, calculated by employing the MLSRK mesh-free method, is plotted at $\Delta z/H_0 = 2\%$ and $\Delta z/H_0 = 4\%$. The value adopted for the so-called dilation parameter, ρ (see [40]), was determined by trial and error ($\rho = 8$). For too low values of ρ, the number of particles within the window is too small and unrealistically irregular strain fields appear. On the contrary, for too large values of ρ, the window region becomes too large to detect any strain localization. From Figure 10(a), it emerges that at $\Delta z/H_0 = 2\%$, the local variation of axial strain from the value of the nominal strain is small, and the strain field of the specimen is still uniform. Conversely, after the drop of axial stress has taken place, (Figure 10(b)), a compaction band perpendicular to the direction of compression is visible in the middle of the sample with the strain field being clearly nonuniform. Experimental tests from the literature usually show compaction bands starting in the vicinity of the platens, because of the presence of tangential stresses caused by friction [3]. However, in our numerical simulations, all the boundary walls are frictionless, so that the onset of the compaction bands is governed only by the heterogeneities initially present in the samples which, owing to the adopted procedure of particle and bond generation, are randomly distributed in space.

Local axial strains were also calculated by means of a second method. The sample was subdivided into 26 layers of thickness approximately equal to one macro-void diameter. The thickness adopted for the layers was determined by trial and error: for higher values of thickness the compaction band could be missed, whereas for lower values an unrealistically irregular strain field would be obtained. In Figure 11, the average axial strains calculated for each layer are plotted before the stress peak (at $\Delta z/H_0 = 2\%$) and afterwards (at $\Delta z/H_0 = 4\%$). It can be observed that inside the compaction band, the axial strain increases sharply to values significantly higher than the imposed nominal strain. In fact, because of the irreversible rearrangements of several unbonded particles, irrecoverable (plastic) deformations take place, whereas outside the band, particles are still bonded, so that the material undergoes elastic unloading. Looking at Figures 10 and 11, it emerges that the fields of axial strain determined by the two different methods, both inside and outside the compaction band, are in a very good agreement regarding both the value of calculated strain and the position of the borders of the compaction band.

3.3. Influence of the damage parameter ω (damage parallel bond model)

From the results of paragraph 3.1, it can be concluded that viscous damping is not effective in regularising the post-peak regime, whereas local damping is. These forms of damping were originally introduced in the DEM with the purpose of either speed up computations or regularising the mechanical response of the sample (e.g. dampening oscillations) but without a direct physical relation to any micromechanical phenomenon causing energy dissipation, hence, calibration of their values is performed on the basis of the desired overall mechanical response of the specimen of granular material rather than to reproduce any experimental measurement, however, currently unavailable, of
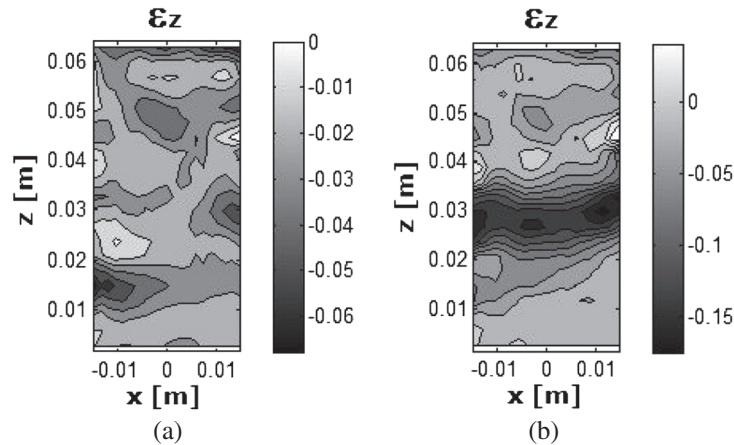

Figure 10. Plots of the vertical strain field within the sample (test SPBl07κ2_2) calculated on a planar slice, xz plane, of the cylindrical sample for: (a) $\Delta z/H_0 = 2\%$ and (b) $\Delta z/H_0 = 4\%$.
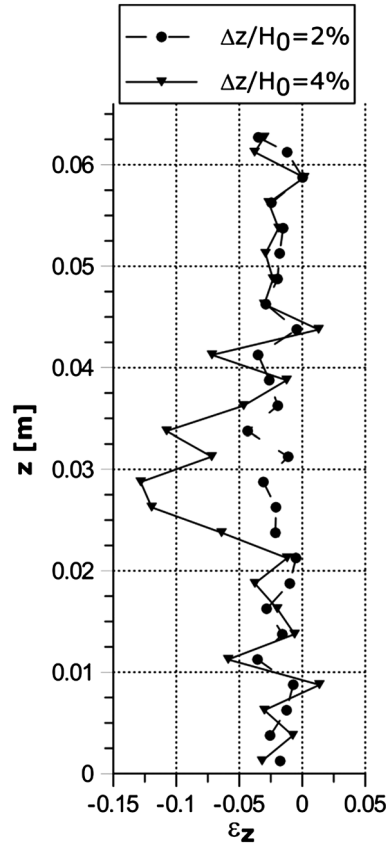
Figure 11. Vertical strain within the samples for different values of $\Delta z/H_0$ in test SPBl07κ2_2. The sample was subdivided into 26 layers. Each symbol represents the average vertical strain within a layer.

dissipative phenomena occurring at the level of grain interaction. Therefore, although damping parameters affect the ductility of the system, they are not related to the ductility of the bonds and do not possess a clear physical meaning. Conversely, in case of the DPB model, the ductility of the bonds is directly controlled by the parameter ω, which possesses a clear physical meaning as the rate of bond damage progression (see par. 2.2). The ability of the DPB model to replicate in a realistic way, the damage process occurring in the bonds, is a key advantage over the SPB model. Moreover, progressive damage of the bonds causes irreversible energy dissipation hence having the effect of regularising the mechanical response of the system although in a different way than the two forms of damping employed in the SPB model do. In this section, simulations run with the DPB model, and no damping are presented with the purpose of assessing the capability of the DPB model to capture the main features relative to the onset and propagation of compaction bands in highly porous rocks and cemented soils.

In Figure 12, the typical $\sigma_a - \Delta z/H_0$ and $\sigma_r - \Delta z/H_0$ responses exhibited by specimens with bonds of the DPB model are plotted. For the sake of analysis of the mechanical behaviour exhibited by the specimens, three stages phases for the mechanical response can be identified. In the first stage, bonds remain intact so that the response is linear elastic. The second stage starts with a gradual but progressive deviation of the response from linearity because of the progressive damage undergone by bonds in the specimen. In the following, it will be shown that depending on the value of ω, the branch of the curves in the second stage can exhibit either hardening or softening. During this second stage, a progressive collapse of macro-voids occurs with the material changing its structure from a high porosity material to a low porosity one and therefore its mechanical properties, that is, stiffness and strength. Finally, the third stage starts where a sharp increase in the slope takes place: there, all macro-voids have collapsed and the material stiffness increases (Figure 12). These three phases are also observed in experimental tests on highly porous rocks [3].
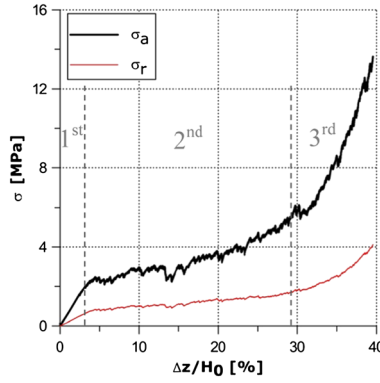
Figure 12. $\sigma_a - \Delta z/H_0$ and $\sigma_r - \Delta z/H_0$ curves obtained for the DPB model (test DPB07κ2_2). The approximate borders of the stages of the mechanical response are marked by dashed grey vertical lines.

The force–displacement relationship obtained for a single bond tested under uniaxial compression is plotted in Figure 13(a), for three values of ω: ω = 0.8, ω = 0.6 and ω = 0.4 (tests DPB07κ2_1, DPB07κ2_2 and DPB07κ2_3). An analogous force–displacement curve scaled down of 10 times in value is obtained in case of uniaxial tension. Note that ω does not affect the strength but only the post-peak strain softening phase of the mechanical response of the bond with the highest ductility for $\omega = 1.0$, that is, relative displacements occurring with the contact force being constant, and the lowest ductility for $\omega = 0.0$, that is, elasto-fragile behaviour without any softening. In Figure 13(b), the curves of axial stress versus nominal axial strain, for samples featured by the aforementioned values of ω ($\omega = 0.8$; $\omega = 0.6$; $\omega = 0.4$), are plotted. In all the curves, a progressive loss of stiffness is noticeable. The deviation of the curve from linearity reflects the fact that bonds start to undergo damage: in all the curves stress drops are visible. The magnitude of the observed drops is highly affected by the amount of ductility adopted for the bonds: the higher the ductility (i.e. the lower the value of ω) is, the lower the stress drops turn out to be and the more ductile the global mechanical response of the system becomes. It is remarkable to note that in case of high ductility of the bonds ($\omega = 0.4$), an overall ductile branch of the curve is obtained with very small stress drops. This shows that the onset of the compaction band can take place even in the presence of an overall ductile behaviour. This is due to the
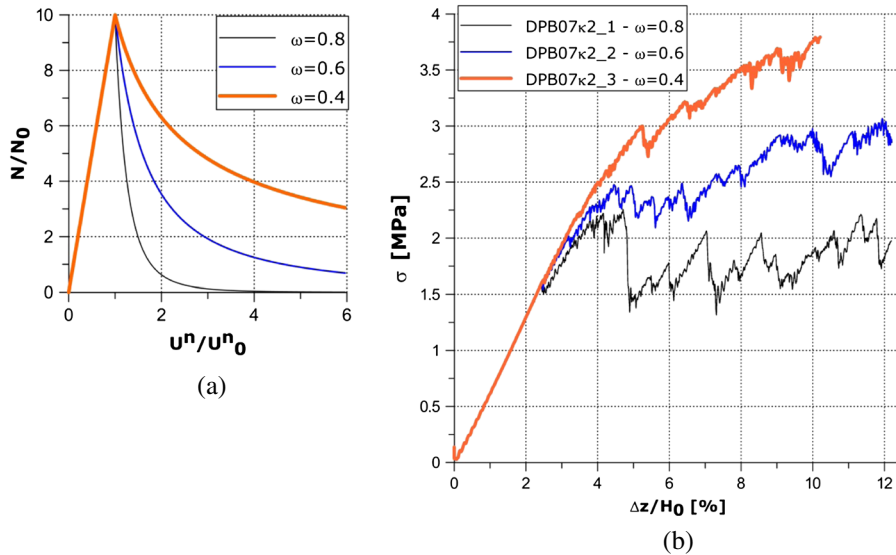

(a)

(b)

Figure 13. (a) Constitutive relationship of the parallel bond in the normal direction and (b) comparison between the $\sigma_a - \Delta z/H_0$ curves obtained in test DPB07κ2_1, DPB07κ2_2, DPB07k2_3.

fact that the collapse of the macro-voids occurs gradually with the grains in the forming compaction band that are moving away from each other and at the same time being held together by damaged but still intact bonds. Later on (see par 4.3), the influence of the size of the macro-voids is also investigated. It will be shown that in case of larger sizes, the macro-voids are so big that their collapse cannot take place without full detachment of the grains taking place (i.e. bond breakage occurring), which leads to significant accelerations on the grains and in turn to a drop of the axial stress.

From Figure 13, it also emerges that the value of ω is strongly related to the amount of the observed stress drops. Intuitively, it can be expected that the ductility of the bonds is related to the global ductility exhibited by the sample, so that the more fragile the bonds (the higher ω), the more fragile is the mechanical response of the specimen. So the amplitude of the observed stress drops increases with ω increasing, that is, with the fragility of the bonds increasing, because the more fragile the bonds the less energy is dissipated by bond damaging and the higher is the portion of energy inputted in the system, via the motion applied to the platens, that is transferred in the form of kinetic energy to the debonded particles whose inertial forces give rise to the drop of nominal axial stress in the specimen. A theoretical analysis on the ductility/brittleness of the system will follow in Section 4. Finally, from Figure 13, we can also note that the difference in terms of nominal axial strain between two consecutive stress drops decreases with ω decreasing, that is, with the ductility of the bonds increasing, which implies an increase in the capability of the system to redistribute contact forces leading to an overall hardening behaviour.

The curve obtained for $\omega = 0.6$ (test DPB07κ2_2) is qualitatively the most similar to the experimental axial stress – axial strain curve reported in Castellanza, *et al.* [3] for a Pumice stone (Figure 14) providing an indication of a realistic value for the damage progression parameter. A quantitative match with the experimental curve could be easily obtained by calibrating the other micromechanical parameters ruling the contact law (Table I). However, fine-tuning of the values of the micromechanical parameters to reproduce a particular experimental curve is not the aim of the paper, which is rather to run a parametric investigation of the influence of the main micromechanical quantities on the formation of compaction bands in cemented granular geomaterials to come up with a deeper understanding of the phenomenon and a theoretical analysis of it. So, it has been shown that the DPB model is a suitable bond model to capture the behaviour of very porous rocks and cemented soils subject to compaction banding having the advantage of being ruled by only one parameter of clear physical meaning whose value can be ascertained by running an oedometric test. For this reason, this model was chosen to perform the parametric analysis presented in Section 4.

In order to investigate the relationship between the onset of compaction bands and the progression of damage in the bonds, in Figure 15, the spatial distribution of broken and damaged bonds is plotted for the three tests run at different values of nominal axial strain (DPB07κ2_3, DPB07κ2_1 and DPB07κ2_2). The cross symbols refer to severely damaged bonds, with the damage variable being $D > 0.5$, whilst the dots refer to broken bonds. First, let us compare simulations for low and high values of ω, that is, $\omega = 0.4$ and $\omega = 0.8$, respectively. At any stage of the test run for low ω values (Figure 15 (a), (b) and (c)), the number of severely damaged bonds is largely greater than the number of broken bonds. The contrary holds true for the test run for high ω (Figure 15(d), (e) and (f)) where the number
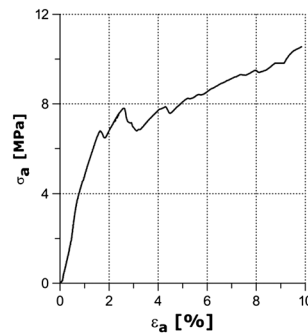

Figure 14. Experimental results obtained on a pumice stone (porosity 70 %) after Castellanza *et al.* [3].
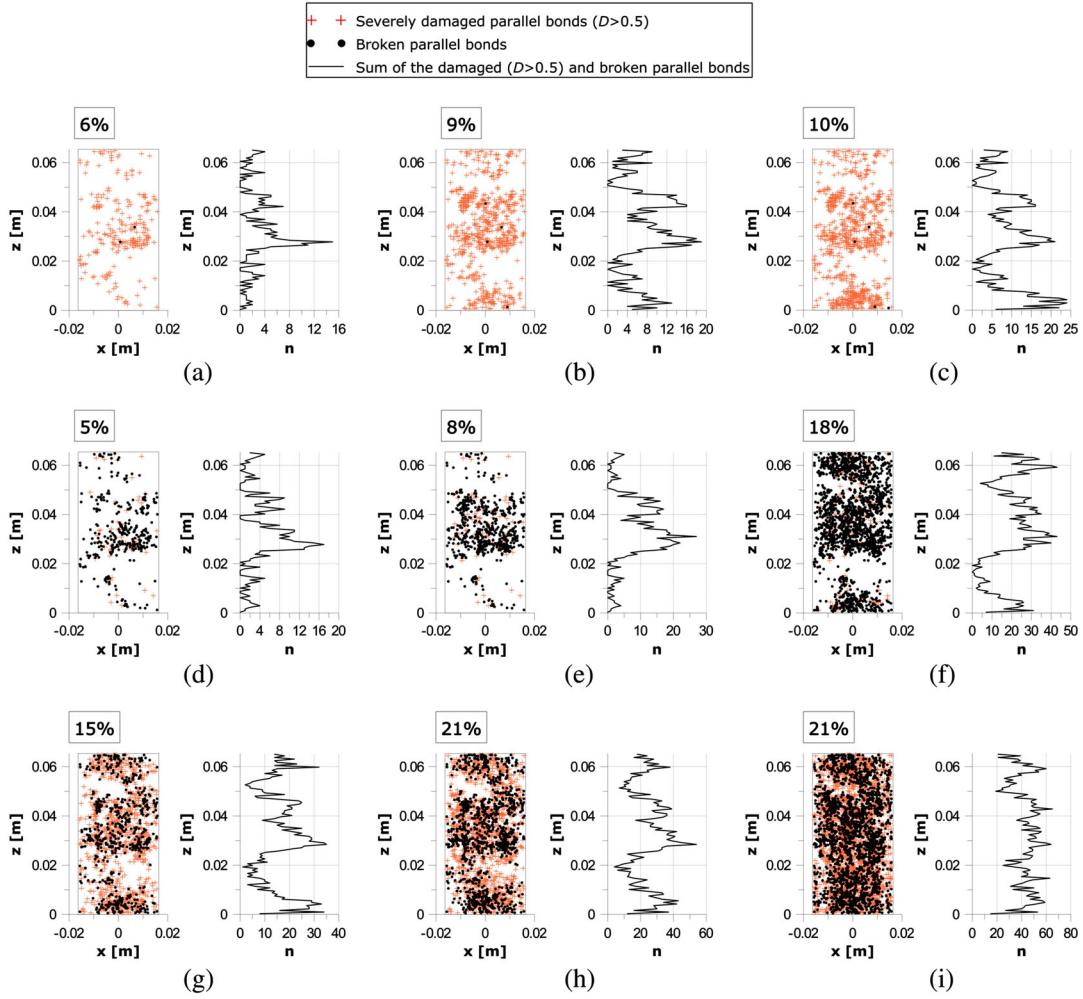
Figure 15. Spatial distribution of damaged and broken bonds within the specimens for various values of ω at different times: (a) $\Delta z/H_0 = 6\%$ for $\omega = 0.4$; (b) $\Delta z/H_0 = 9\%$ for $\omega = 0.4$; (c) $\Delta z/H_0 = 10\%$ for $\omega = 0.4$; (d) $\Delta z/H_0 = 5\%$ for $\omega = 0.8$; (e) $\Delta z/H_0 = 8\%$ for $\omega = 0.8$; (f) $\Delta z/H_0 = 18\%$ for $\omega = 0.8$; (g) $\Delta z/H_0 = 15\%$ for $\omega = 0.6$; (h) $\Delta z/H_0 = 21\%$ for $\omega = 0.6$; and (i) $\Delta z/H_0 = 31\%$ for $\omega = 0.6$.

of severely damaged bonds is negligible in comparison with the number of broken bonds. In the intermediate case of $\omega = 0.6$ (Figure 15(g), (h) and (i)), the number of severely damaged and broken bonds is approximately of the same magnitude, which is consistent with the behaviour observed in the other two cases of high and low ω values. Moreover, it can be derived that the thickness of the compaction band is related to the value of ω with compaction bands being thinner at low values of ω.

Concerning the sequence of formation of the compaction bands, it can be noted that localizations arise in several zones of the specimen until full compaction is reached (Figure 15(g)). In all the tests, the presence of a second band just above the first one can be observed (Figure 15(a), (d) and (g)). Subsequently, at higher nominal average axial strains, a third and fourth band develop near the top and bottom boundaries, respectively (Figure 15(f) and (h)).

4. PARAMETRIC ANALYSIS

In the previous section, it has been shown that the DPB model is a suitable bond model to qualitatively capture the mechanical behaviour of very porous rocks and cemented soils subject to compaction banding due to bond destructuration. The DPB model has the advantage of being ruled by only one

parameter, ω, of clear physical meaning (i.e. the bond damage rate). In the following, the main factors affecting the mechanical response of the studied geomaterials are investigated, in particular:

    (i) the influence of initial porosity on the inclination of compaction bands;

   (ii) the occurrence of phenomena of global instability; and

  (iii) the influence of the size of macro-voids.

4.1. Influence of porosity

In order to assess the influence of porosity on the mechanical response of the system, numerical tests for a value of initial porosity lower than the value adopted in the previous section, $n = 0.5$ and $n = 0.6$, were run. The grain size distribution and the size of macro-voids, $\kappa = 2$, were the same as in the previous tests. Because of the lower porosity, fewer macro-voids (e.g. $N_m = 520$) were generated in these tests. For these lower values of porosity, localization is observed only if high enough values of ω are adopted (no localisation for $\omega = 0.6$ and localisation for $\omega = 0.8$). This can be explained considering that lower porosity implies a higher number of bonds per grain, hence, an overall more stable structure so that the structure becomes unstable only in case of high fragility of the bonds.

From the simulations, the existence of a threshold value of porosity, around $n = 0.6$, below which there is the formation of a band of localised damaged whose inclination is no longer horizontal but oblique. The lower the porosity is, the more inclined the band is. In Figure 16(a), the $\sigma_a - \Delta z/H_0$ and $\sigma_r - \Delta z/H_0$ curves of test DPBv05κ2_2, with $n = 0.5$, are plotted. The occurrence of instability is signalled by a sharp drop in the monitored stresses taking place at $\Delta z/H_0 = 9\%$. In Figure 16(b), the spatial distribution of the broken bonds at $\Delta z/H_0 = 9\%$ is plotted. Unlike previous tests run for $n = 0.7$, the region where the broken bonds are concentrated in a band whose normal is inclined of 45 over the x-axis and 34 over the y-axis. The band propagates vertically; therefore, the direction of propagation does not coincide with the normal to the plane of the band as in the case of pure mode compaction bands.

The mechanical coordination number relative to the specimen here considered ($C_N^{pb} = 4.72$) is significantly higher than that relative to tests in SPBl07κ2_2 and SPBv07κ2_2, leading to a specimen with higher stiffness and strength, owing to the presence of a larger number of bonds. As a consequence, at the onset of localisation, the stress ratio, $\eta = q/p$, with $q = \sigma_a - \sigma_r$, the deviatoric stress and $p = (\sigma_a + 2\sigma_r)/3$, the mean effective pressure, is 10% higher ($\eta = 1.3$ in test SPBv07κ2_2 and $\eta = 1.45$ in test SPBv05κ2_1) than in tests SPBv07κ2_2 and SPBv05κ2_1. This observation further corroborates what was already stated by Rudnicki [44], about the effect of stress anisotropy on the onset of mixed modes of localisation (mixed between compaction and shear bands): 'the
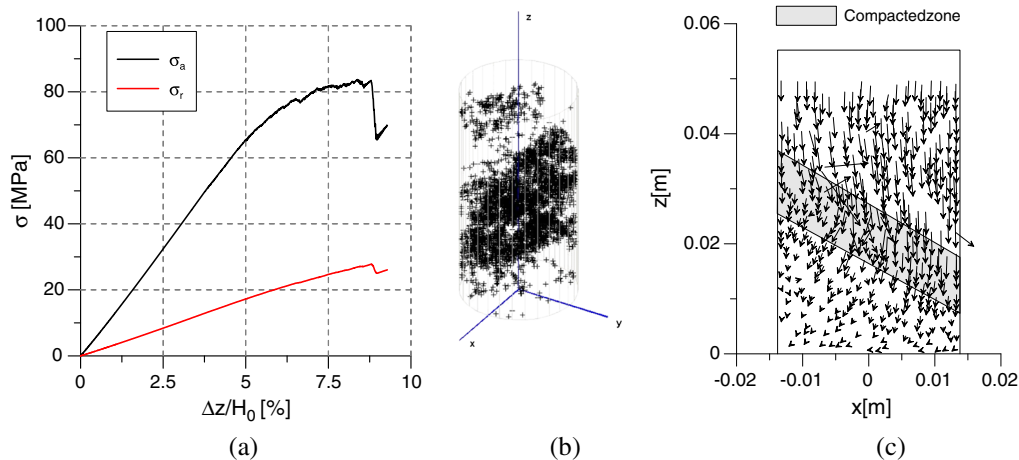

Figure 16. Test DPBv05κ2_2 for $n = 0.5$: (a) $\sigma_a - \Delta z/H_0$ and $\sigma_r - \Delta z/H_0$ curves; (b) 3D view of the location of the broken bonds (test DPBv05κ2_2); and (c) velocity vectors of some balls belonging to a planar slice (plane xz) of the sample.

analyses of Issen and Rudinicki [45, 46] suggest that small variations in material parameters may favour the appearance of either shear or compaction bands. Bésuellle [47] has shown that the results of Rudinicki and Riece (1975) predict that the mode of deformation in the localised (shear versus dilatation or compression) varies continuously between pure compaction and pure dilatation'. In fact, a sample of lower porosity is featured by more bonds at generation, hence, higher strength; therefore, the loss of linearity in the stress–strain curve (yield point) corresponding to the occurrence of irreversible deformations takes place for a higher value of the stress ratio, η. This value is higher than the stress ratio marking the transition between fragile and ductile behaviour but lower than the threshold value required for the occurrence of pure shear bands. Therefore, for η in this range, mixed modes of localisation take place [44].

4.2. Brittleness of the system

Figures 16(a) and 17(a), referring to tests DPBv07κ5_1 and DPB05κ2_2, respectively, show the occurrence of a globally unstable behaviour, that is, a vertical drop in the nominal axial stress. In the previous section, it has been shown that the amount of stress drop is related to how quickly a compaction band develops and propagates within the specimen. To investigate the phenomenon further, the specimen of test DPBv07κ2_2 (Figure 17(a)) was subdivided into 9 layers. Axial and radial stresses were calculated for each layer. The radial stress of each layer was determined as the sum of the normal contact forces against the cylindrical wall divided by the lateral area of the layer. The vertical stress of each layer instead was calculated as the average between the stresses acting at its top and bottom interface. In order to determine the vertical stress acting on the boundary of each layer, first, the inertial force acting on each layer was calculated as the sum of the inertial forces acting on the particles of the layer; second, vertical dynamic equilibrium was imposed for each layer in succession starting from the uppermost layer with the stress at the upper boundary given by the reaction force exerted by the top platen divided by the platen area. Axial and radial stresses were evaluated at regular discrete intervals of nominal axial strains of the sample (see the markers in Figure 17(a)).

In Figure 18, $\sigma_a - \varepsilon_z$ and $\sigma_r - \varepsilon_z$ curves calculated for three representative layers are plotted. The layers considered are the following: layers 8 and 9 where the specimen undergoes localisation and layer 2 representative of the part of the sample outside the localised region. All the curves exhibit the initial linear trend typical of the elastic stage of the material when all bonds are intact. However, taking the
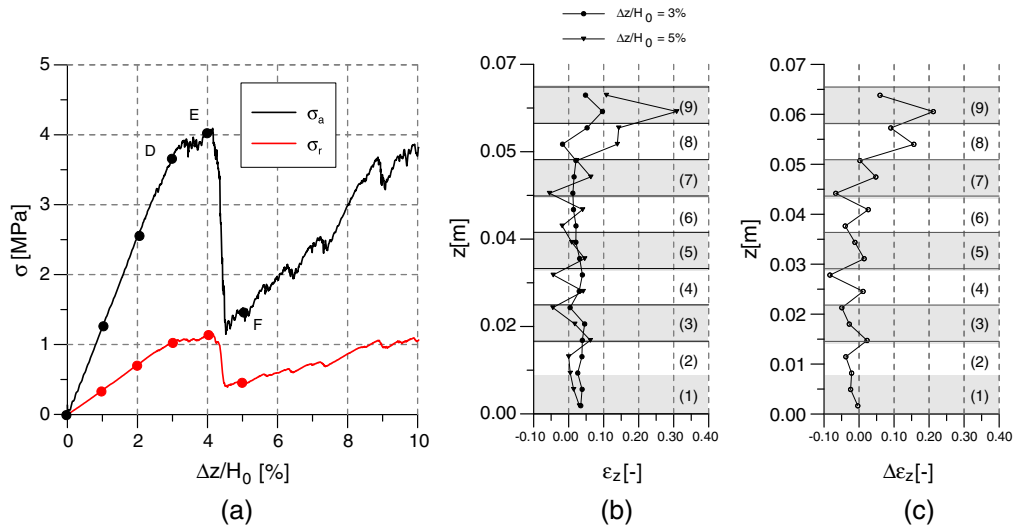

Figure 17. Test DPBv07κ5_1: (a) $\sigma_a - \Delta z/H_0$ and $\sigma_r - \Delta z/H_0$ curves; (b) axial strains calculated per each layer at the end of the linear elastic stage ($\Delta z/H_0 = 3\%$) and after the snap-back ($\Delta z/H_0 = 5\%$); and (c) increment of axial strain per layer between $\Delta z/H_0 = 3\%$ and $\Delta z/H_0 = 5\%$.
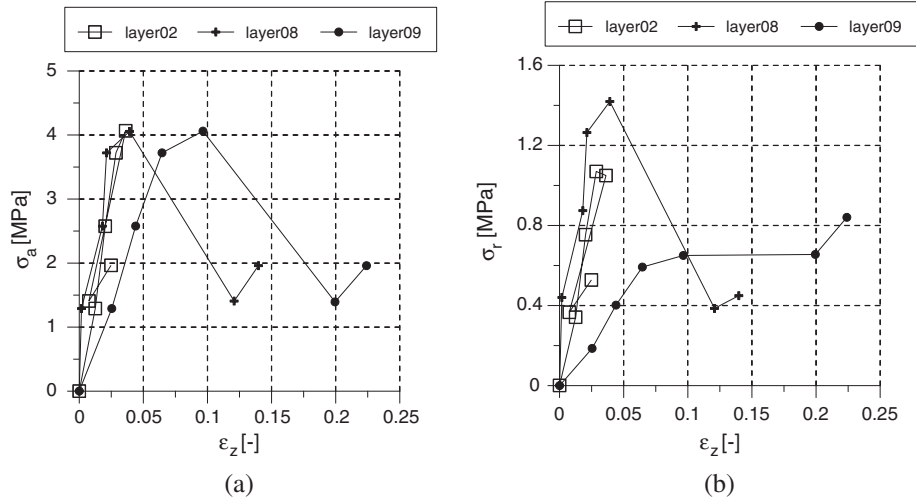
Figure 18. Test DPBv07κ5_1: stresses versus axial deformation calculated in layer 2 (squares), representative of the non-localised part of the sample, and layers 8 and 9 (crosses and full circles, respectively), which are subject to localization: (a) layer axial stress, σ_a, versus layer axial strain, ε_z; and (b) layer radial stress, σ_r, versus layer axial strain, ε_z.

initial slope of the curves into consideration, a slight difference is apparent. This is probably because of the fact that the layer size is significantly smaller than the specimen size (around one-tenth); hence, it is smaller than the REV size calculated in Section 2 (Figure 4). The recorded value of the stress peak is the same for all the curves and coincides with the value measured at the specimen boundaries (Figure 17(a)). After the stress peak is reached, layers 1, 2, 3, 4, 5, 6 and 7 (Figure 18(a) and (b)) undergo elastic unloading during the development of the compaction band. Conversely, the stress paths computed for layers 8 and 9, where the compaction band develops, show that a sort of strain softening occurs (Figure 18(b)). The fall in the axial stress observed for layers 8 and 9 can be explained with the fact that the unloading of the elastic domain outside the compaction band is not large enough to compensate for the displacement generated by the compaction band. After the compaction band has formed ($\Delta z/H_0$ =5%), all layers undergo further elastic loading from $\Delta z/H_0 = 5\%$ to $\Delta z/H_0 = 6\%$ (see the upward linear trends in the final part of all the axial stress–axial strain curves in Figure 18(a) and radial stress–axial strain curves in Figure 18(b)).

4.3. Influence of the macro-void size

So far, it has been shown that compaction banding is due to the collapse of macro-voids; hence, in this section, we want to investigate the influence of the macro-void size on the formation of compaction bands. To this end, tests relative to two specimens with different macro-voids sizes but with similar coordination number (Table II) were run with all micromechanical parameters for the two specimens being equal apart from parameter κ, indicating the size of macro-voids. The $\sigma_a - \Delta z/H_0$ curves of test DPB07κ5_1 ($\phi_m = 6.13$ mm, $\kappa = 5$) and test DPB07κ2_2 ($\phi_m = \phi_1 = 2.5$ mm, $\kappa = 2$) are compared in Figure 19. It emerges that the increase in the diameter of the macro-voids implies (i) an increase in the initial oedometric modulus, E_{oed}, of 49%; (ii) an increase in the axial peak stress of 39%; and (iii) an overall marked increase in the global brittleness because the drop of axial is far more abrupt. Instead, the value of $\Delta z/H_0$ at the occurrence of the first peak is similar. The second phase of the $\sigma_a - \Delta z/H_0$ curve is featured by less frequent but more pronounced oscillations of the axial stress, which are due to the larger size of the macro-voids employed.

Because the two artificial materials are characterised by the same density, grain size distribution and micromechanical constitutive parameters, the different mechanical behaviour exhibited by the two numerical specimens has to be ascribed to the difference in the two internal microstructures. The pore size distribution of the DEM cylindrical samples is a bimodal distribution with two dominant pore modes: the first is relative to the macro and the second to the micro-pores, respectively. Because the
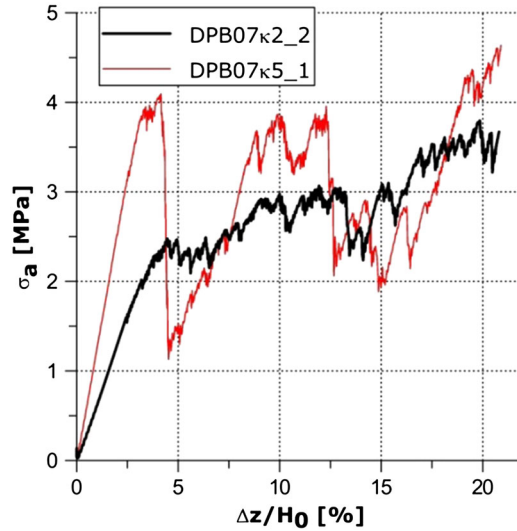
Figure 19. $\sigma_a - \Delta z/H_0$ curves obtained for test DPB07κ2_2 and test DPB07κ5_1.

global porosities of the two samples coincide, this implies that their pore size distributions differ. Given the reduction in micro-porosity, relative to specimens DPB07κ5_1, the regions of specimen around macro-voids are denser: this causes the observed global increase in strength, stiffness and brittleness of the system.

Now, each localization phenomenon can be related to a characteristic length for the material, which governs the extension of the localization taking place. Hence, it is desirable to identify the characteristic length for the bond breakage induced compaction bands taking place in the porous materials, featured by a bimodal distribution of pores, here investigated. To this end, the increment of axial deformation along the vertical axis, between pre localization and post localization for the two tests, here examined (κ = 2 and κ = 5) were calculated via the method illustrated in Section 2 and plotted in Figure 20. Hatched bands were drawn to highlight the

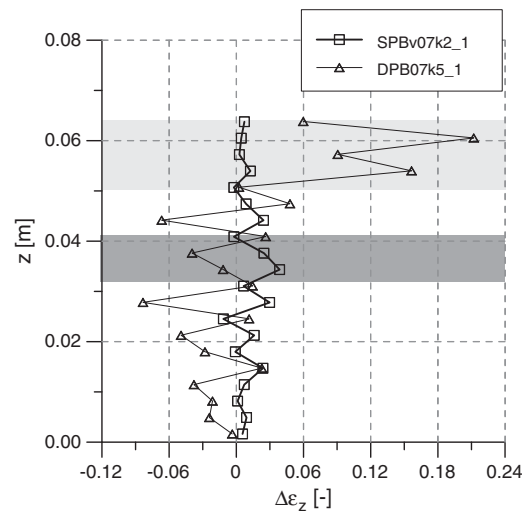Figure 20. Increment of axial deformation occurring during localization, between 3% and 21%, along the specimen for test DPB07k2_2, with k = 2 and test DPB07k5_1, with k = 5. Each symbol, triangles or squares, indicates the value of incremental deformation calculated in a layer via the simplified method (20 layers were used for this purpose). The hatched regions indicate the location of the compaction bands.

regions where compaction banding took place: the darker band indicates the presence of the compaction band for the sample with smaller macro-void ($\kappa = 2$) whilst the lighter band for the sample with larger macro-voids ($\kappa = 5$). Comparing the sizes of the two bands, it emerges that they are roughly in the same proportion as the size of their macro-voids, that is, there is a ratio of roughly 2.5 times. This observation indicates that the size of the macro-void could be taken as an approximate measure of the characteristic length of the material for the occurrence of compressive compaction bands. Moreover, from Figure 19 emerges that the brittleness of the global mechanical response is affected by the characteristic length of the material.

5. CONCLUDING REMARKS

This paper investigated both the onset and the propagation of compressive compaction bands in an ideal highly porous material under oedometric conditions via 3D DEM analyses carried out on cylindrical samples. The material has been modelled as a collection of bonded grains with several macro-voids randomly distributed. This ideal material is evidently inspired by a large class of natural/artificial porous geomaterials (e.g. natural cemented soils and artificial conglomerates) where (i) a granular structure can be recognised and (ii) the bridges sticking the grains together act as predefined points of weakness.

Two different bond models were employed to describe the process: an elasto-brittle model based on PFC current bond models, and a more sophisticated elasto-damage model conceived by the authors to simulate more realistically the process of bond degradation. The obtained results show that compaction bands can be triggered by the breakage of bonds, leading to the collapse of several macro-voids in the specimen, without any grain crushing taking place.

Moreover, it was shown that if the elasto-brittle model is employed, the observed mechanical behaviour of the specimens, in terms of peak strength, brittleness and onset and propagation of localisation, depends on the values of damping adopted even in case of tests run under quasi-static conditions. Calibration of meaningful values of damping is very difficult because currently there are no experimental measurements able to link bond properties (e.g. ductility) to values of damping coefficients. In the elasto-damage model introduced by the authors instead, no damping is employed but the progression of bond failure, that is, bond ductility, is controlled by a parameter of clear physical meaning: the rate of bond damage progression, ω. Then, the DPB model has shown to be a suitable model to qualitatively capture the behaviour of very porous weak rocks and cemented soils. The rate of bond damage progression has been found to affect both the onset and extension of compaction bands and the overall brittleness/ductility of the numerical specimens.

Oedometric tests for different values of porosity were run. Below a certain threshold of porosity, the onset of mixed modes of localisation, between a shear and a compaction band, was observed. In this case, the direction of propagation of the band is no longer orthogonal to the band boundaries because of the presence of both axial and shear strains. The state of stress calculated in the samples showed to be in qualitative agreement with the theoretical conditions for the onset of mixed modes under axial-symmetric conditions established by [44].

Tests for the different values of macro-void size were performed with the overall density of the material, grain size distribution and all the micromechanical constitutive parameters kept constant: stiffness, strength and ductility exhibited a dramatic change. When the size of the macro-voids is increased, it was observed that snap-back is favoured because the ratio between the material characteristic length and the specimen height is decreased. This conclusion supports the idea that, when such a phenomenon takes place, the rate of propagation of the compaction band can no longer be controlled by the displacement of the specimen platens. It was also shown that, in case of double porosity materials and in the absence of grain crushing, the characteristic length of the material with regard to the occurrence of compaction bands seems to be related to the size of the macro-voids. However, there is no sufficient evidence to exclude that grain size or some other material properties may have a stronger influence on the characteristic length of the material.

6. NOTATION

SCALARS

A	parallel bond area
$A_{\min}$	minimum parallel bond area
$A_{\max}$	maximum parallel bond area
C_N^{pb}	mechanical coordination number
D	damage variable
E_k	kinetic energy
E_{oed}	oedometric modulus
F^{up}	modulus of the vertical force acting on the upper platen
F^{dw}	modulus of the vertical force acting on the lower platen
H_0	initial height of the sample
I	parallel bond moment of inertia
J	parallel bond polar moment of inertia
K^n	normal secant contact stiffness
M	generalised bending moment
$\overline{M}$	third internal variable
M_0	initial value of the third internal variable
M_t	generalised torque moment
N	generalised axial force
$\overline{N}$	first internal variable
N_0	initial value of the first internal variable under traction
$\widetilde{N}_0$	initial value of the first internal variable
N_m	number of macro-voids
N_p	number of micro-particles
$\overline{R}$	parallel bond radius
V	generalised shear force
U^n	component of the normal relative displacement between two particles along the unit vector normal to the contact plane
U^s	component of the shear relative displacement between two particles along the unit vector tangent to the contact plane
$\overline{V}$	second internal variable
V_0	initial value of the second internal variable
V_{0L}	initial volume of a layer
V_{sL}	volume of solids in a layer
V_{s0L}	initial volume of solids in a layer
V_t	volume of the specimen
V_s	solid fraction of volume
V_{vL}	volume of voids in a layer
c_N^{pb}	standard coordination number
e_L	void index of a layer
$g(\mathbf{Q},\chi,D)$	threshold function
$\underline{g(\mathbf{Q},\chi,D)}$	
$\overline{k}^n$	normal parallel bond stiffness
k_n^p	normal particle stiffness
k_n^w	normal wall stiffness
k^s	tangential contact stiffness
k_s^p	tangential particle stiffness
k_s^w	tangential wall stiffness
$\overline{k}^s$	tangential parallel bond stiffness
n	porosity of the sample
p	mean effective pressure

q	deviatoric stress
Δz	vertical displacement of the upper platen of the sample
α	ratio between the height and diameter of the sample
β_n	normal critical damping ratio
β_s	shear critical damping ratio
δ	coefficient of Cundall's damping
ε_{volL}	average volumetric strain of a layer
ε_z	vertical strain
ε_{zL}	average vertical strain of a layer
η	ratio between deviatoric stress and mean effective pressure
θ^n	component of the normal relative rotation between two particles along the unit vector normal to the contact plane
θ^n	component of the shear relative rotation between two particles along the unit vector tangent to the contact plane
$\dot{v}$	nominal axial strain rate
ξ_1	parameter of DPB model
ξ_2	parameter of DPB model
ϕ_m	diameter of macro-voids
ϕ_1, ϕ_2	diameters of macro-voids used in the simulations
ϕ_p	diameter of a particle
$\phi_{p,max}$	maximum diameter of micro-particles
$\phi_{p,min}$	minimum diameter of micro-particles
$\phi_{p,mean}$	mean radius of micro-particles
Δ	diameter of the sample
κ	ratio between macro-voids diameter and mean micro-particle diameter
μ	friction coefficient at the contact
μ^p	inter-particle friction coefficient
μ^w	wall friction coefficient
ρ_p	density of the particles
ρ	dilatation parameter for MLSRK mesh-free method
σ_0	maximum value of normal stress (DPB model)
σ_a	axial stress
$\overline{\sigma}_c$	normal strength of the parallel bond (SPB model)
σ_r	radial stress
$\overline{\tau}_c$	shear strength of the parallel bond (SPB model)
τ_0	maximum value of shear stress (DPB model)
ω	parameter governing the rate of damage

VECTORS

$\overline{\mathbf{F}}^n$	axial force acting on a parallel bond
$\overline{\mathbf{F}}^s$	shear force acting on a parallel bond
$\overline{\mathbf{M}}^s$	torque moment acting on a parallel bond
$\overline{\mathbf{M}}^n$	bending moment acting on a parallel bond
$\mathbf{Q}$	vector collecting the generalised forces and moments on the parallel bond
$\widetilde{\mathbf{Q}}$	effective generalised forces and moments vector
$\mathbf{U}^s$	shear relative displacement between two particles
$\mathbf{g}_i$	unit vector defining the direction of the discontinuity of the strain rate field
$\mathbf{n}$	unit vector normal to the contact plane between two particles
$\mathbf{n}_i$	unit vector perpendicular to the localization plane
$\mathbf{q}$	vector collecting the generalised relative displacement and rotations between two particles
$\mathbf{r}$	unit moment vector tangent to the contact plane between two particles
$\mathbf{s}$	unit shear vector tangent to the contact plane between two particles

$\mathbf{\theta}^s$ shear relative rotation between two particles

χ vector of internal variables

TENSOR

$\mathbf{D}^e$ elastic tensor in the damage model

APPENDIX

Implementation of the elastic-damage bond model

In this section, the implementation of the elasto-damage bond model in PFC is presented. At every timestep, forces and moments acting on each bond are calculated by PFC from the relative displacements and rotations of the two bonded particles according to the 'parallel bond' routine. The calculated forces and moments were then adjusted to the values predicted by the law of the elasto-damage bond model presented in Section 2.2 via an ad-hoc routine written by the authors. Referring to Figure A1, the implemented algorithm can be summarised as follows:

1. For each parallel bond at timestep i, the generalised loads Q_i acting on the bond and the damage variable D_i are retrieved from external variables.
2. The new forces acting on each bond, just computed by PFC, are set to zero.
3. Defining $\mathbf{Q}$ as the vector of the generalised loads computed according to the linear elastic force–displacement law, the increment of $\mathbf{Q}$ in the timestep would amount to

$$\Delta\mathbf{Q} = \mathbf{Q}\text{-}\mathbf{Q}_i \tag{A.1}$$

4. Being q_i, the vector of the generalised displacement and rotations

$$\mathbf{q}_i = \mathbf{D}^{e-1}\frac{\mathbf{Q}_i}{(1-D_i)} \tag{A.2}$$

the corresponding increments in the timestep according to the linear elastic law are as follows:

$$\Delta\mathbf{q} = \mathbf{D}^{e^{-1}}\Delta\mathbf{Q} \tag{A.3}$$

with $\mathbf{D}^e$ given by Eqn (9).

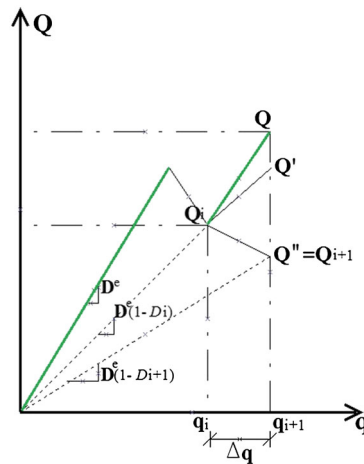5. Hence, displacement and rotations at the new timestep, $i+1$, can be calculated as

Figure A1. Schematic representation of the damage algorithm.

$$\mathbf{q}_{i+1} = \mathbf{q}_i + \Delta\mathbf{q} \qquad (A.4)$$

6. The actions on the *parallel bond* computed considering the damage variable at the previous timestep i

$$\mathbf{Q'} = (1 - D_i)\mathbf{D}^e\mathbf{q}_{i+1} \qquad (A.5)$$

7. The vector $\mathbf{Q'}$ just computed is correct only if the damage has not increased during the timestep.

This means that

$$g(\mathbf{Q'}(D_i), \chi(D_i)) \leq 0 \qquad (A.6)$$

On the contrary, if $g > 0$, the damage has increased during the timestep, and the new damage variable D_{i+1} has to be determined so that the new load point lies on the threshold surface. Thus, the following equation gives the new damage D_{i+1}:

$$g(\mathbf{Q''}(D_{i+1}), \chi(D_{i+1})) = 0 \qquad (A.7)$$

Equation (A.6) is an implicit one and can be solved by adopting the Newton–Raphson algotithm. If D_{i+1} is higher than 0.99, the breakage of the bond is imposed.

8. If D_{i+1} is lower than 0.99, the new actions $\mathbf{Q''}$ on the parallel bond are

$$\mathbf{Q''} = \mathrm{q}_{i+1}\mathrm{D}^e(1 - D_{i+1}) \qquad (A.8)$$

9. The variables $\mathbf{Q''}$ and D_{i+1} are recorded in the array of variables describing the bond state so that they can be retrieved at the following timestep.

VALIDATION OF THE ELASTO-DAMAGE CONTACT MODEL

In the following, the process of validation for the adopted elasto-damage contact model is provided. Let us consider two particles with $\phi_p = 1\,\mathrm{m}$ joined together by both a parallel and a contact bond. In this test, the parallel bond between the particles cannot break, even when the damage variable D exceeds the limit value $D = 0.99$. The two particles are free to move in the (x, z) plane so each ball has three DOF. The DOF of the left ball are fixed. Forces and moments can be applied on the right ball, in order to cause its motion with actions on the parallel bond arising as a consequence.

The DEM parameters employed in these tests are reported in the following table III.

Case of single load

A horizontal force F_x, directed opposite to the x-direction, was applied to the right ball. The force was applied gradually and linearly over time:

$$F_x(t) = -0.25t \qquad (A.9)$$

with t being the time. The consequent motion of the right ball produces an axial force (compression) on the parallel bond. In particular, we want to check the behaviour of the bond for the three different values of ω: 0.3, 0.6 and 0.8. The number of timesteps in the three tests was the same.

Table III. Parameters used for the validation test of the damage model.

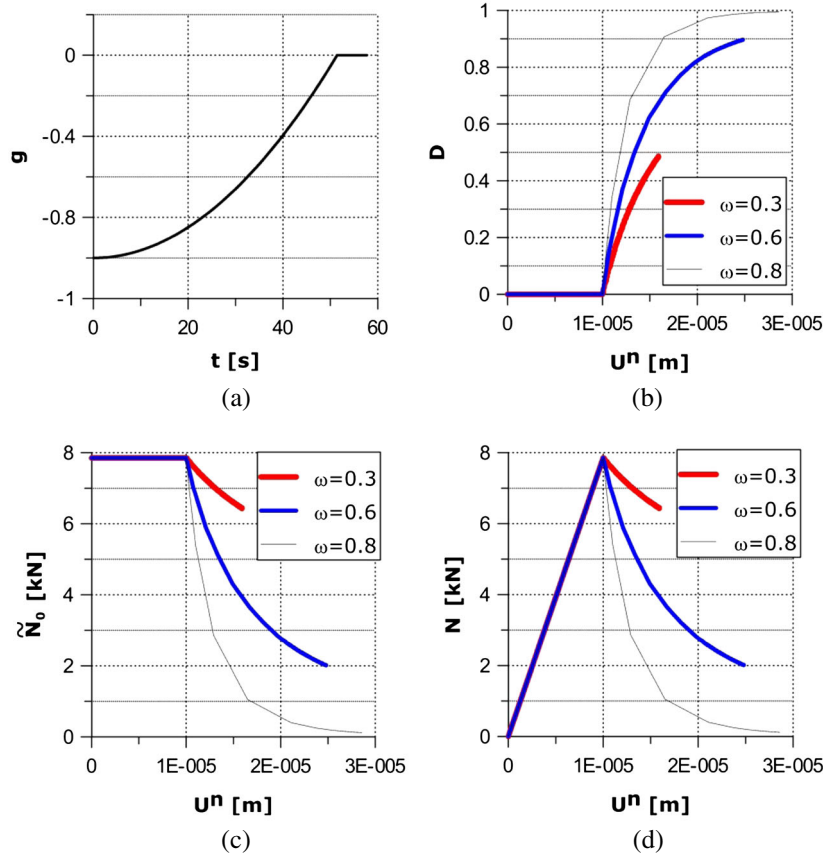| ρ_p [kg/m^3]	k^n [kN/m]	k^s/k^n	$\overline{k}^n$ [kN/m^3]	$\overline{k}^s/\overline{k}^n$	σ_0 [kPa]	τ_0 [kPa]
2650	1 E+6	1	1 E+6	1	1.0	1.0

Figure A2. Validation test of the damage model: (a) load history; (b) evolution of the damage variable with the normal displacement; (c) evolution of the internal variable $\widetilde{N}_0$ with the normal displacement; and (d) normal force–normal displacement curves.

In all the cases, when $t = 51s$, the displacement U^n was equal to 1×10^{-5} m with the force N acting on the parallel bond reaching the limit value $\widetilde{N}_0 = 7.85$ kN, the bond begins to undergo damage. During the subsequent damage process, the value of the threshold function g remains equal to 0 (Figure A2(a))

The graphs in Figure A2(b) show the evolution of the damage variable with the normal displacement. Both the rate of damage and the accumulated displacement U^n increase with ω. When $\omega = 0.8$, the damage is almost complete and D is very close to 1 but this limit value can only be reached asymptotically. The parameter $\widetilde{N}_0$ defines the size of the threshold surface (Figure A2(c)). When the critical displacement is reached, the parameter $\widetilde{N}_0$ decreases with the progress of the damage. The velocity of the shrinkage is as much higher as ω is closer to 1. Finally, the force–displacement graph is plotted in Figure A2(d). After the elastic phase, $N = \widetilde{N}_0$, a softening phase, clearly controlled by ω, follows. The slope of the softening part increases with the increasing of ω, and the softening is more pronounced.

Case of combined load

A vertical and a horizontal force directed opposite to the z-axis and x-axis are applied to the right ball. The relative rotation, in the y-direction, between the two balls is constrained in order to avoid the arising of the bending moment on the parallel bond and to study only the interaction between N and V.

The following loading–unloading histories are relative to the horizontal and vertical force, respectively.

$$F_x(t) = \begin{cases} -0.18t & t \le 60s \\ -10.8 + 0.18(t - 60s) & t > 60s \end{cases} \tag{A.10}$$

$$F_z(t) = \begin{cases} -0.00751t & t \leq 60s \\ -0.4506 + 0.00751(t - 60s) & t > 60s \end{cases} \qquad (A.11)$$

REFERENCES

1. Andriani GF, Walsh N. Petrophysical and mechanical properties of soft and porous building rocks used in Apulian monuments (south Italy). *Geological society, London, Special Publications* 2010; **333**:129–141.
2. Ciantia MO. Multiscale hydro-chemo-mechanical modeling of the weathering of calcareous rocks: an experimental and numerical study. PhD thesis, Politecnico di Milano, Milan, Italy 2013.
3. Castellanza R, Gerolymatou E, Nova R. Experimental observation and modelling of compaction bands in oedometric tests on high porosity rocks. *Strain* 2009; **475**:1–14.
4. De Gennaro M, Cappelletti P, Langella A, Scarpati C. Genesis of zeolites in the Neapolitan Yiellow Tuffs: geological, volcanological and mineralogical evidence. *Contribution to Mineralogy and Petrology*. Springer: 2002; **139**:17–35.
5. Nova R, Parma M. Effects of bond crushing on the settlements of shallow foundations on soft rocks. *Geotechnique* 2011; **61**(3):247–261.
6. Cucino P, Eccher G, Castellanza R, Parpajola A, Di Prisco C. Expanded clay in deep mechanised tunnel boring. *Proc. ITA-AITES World Tunnel Congress Bangkok*, 2012.
7. Porbaha A. State of the art in deep mixing technology: part I. Basic concepts and overview. *Ground Improvement* 1998; **2**:81–92.
8. Arroyo M, Castellanza R, Nova R. Compaction bands and oedometric testing in cemented soils. *Soils and Foundations* 2005; **45**(2):181–194.
9. Horpibulsuk S, Bergado DT, Lorenzo GA. Compressibility of cement admixed clays at high water content. *Geotechnique* 2004; **54**:151–154.
10. Lorenzo GA, Bergado DT. Fundamental characteristics of cement-admixed clay in deep mixing. *Journal of materials in civil engineering ASCE* 2006; **18**:161–174.
11. Nagaraj TS, Pandian NS, Narasimha Raju PSR. Compressibility behaviour of soft cemented soils. *Geotechnique* 1998; **48**:281–287.
12. Horpibulsuk S, Miuara N, Nagaraj TS. Assessment of strength development in cement-admixed high water content clays with Abram's law as a basis. *Geotechnique* 2003; **53**:439–444.
13. Mollema PN, Antonellini MA. Compaction bands: a structural analog for anti-mode I cracks in aeolian sandstone. *Tectonophysic* 1996; **267**:209–228.
14. Eichhubl P, Taylor WL, Pollard DD, Aydin A. Paleo-fluid flow and deformation in the Aztec Sandstone at the Valley of Fire, Nevada-Evidence for the coupling of hydrogeological, diagenetic and tectonic processes. *Geological Society of America Bulletin* 2004; **116**(9–10):1120–1136.
15. Sternlof KR, Pollard D. Numerical modeling of compactive deformation bands as granular "anti-cracks". *Eos, Transactions American Geophysical Union* 2002; **83**(47):T11F–10.
16. Sternlof KR, Rudnicki JW, Pollard DD. Anticrack-inclusion model for compaction bands in sandstone. *Journal of Geophysical Research – Solid earth* 2005; **110**:B11403.
17. Olsson WA. Theoretical and experimental investigation of compaction bands in porous rock. *Journal of Geophysical Research* 1999; **104**(B4):7219–7228.
18. Olsson WA, Holcomb DJ. Compaction localization in porous rock. *Geophysical Research Letters* 2000; **27**(21):3537–3540.
19. Wong T, Baud P, Klein E. Localized failure modes in a compactant porous rock. *Geophysical Research Letters* 2001; **28**(13):2521–2524.
20. Klein E, Baud P, Reuschle T, Wong T. Mechanical behaviour and failure mode of Bentheim sandstone under triaxial compression. *Physics and Chemistry of the Earth* 2001; **26**(1–2):21–25.
21. Vajdova V, Wong T. Incremental propagation of discrete compaction bands: acoustic emission and microstructural observations on circumferentially notched samples of Bentheim sandstone. *Geophysical Research Letters* 2003; **30**(14):1175.
22. Baud P, Klein E, Wong T. Compaction localization in porous sandstones: spatial evolution of damage and acoustic emission activity. *Journal of Structural Geology* 2004; **26**:603–624.
23. Katsman R, Aharonov E, Scher H. Numerical simulation of compaction bands in high porosity sedimentary rock. *Mechanics of materials* 2005; **37**:143–162.
24. Wang B, Chen Y, Wong T. A discrete element model for the development of compaction localization in granular rock. *Journal of Geophysical Research – Solid earth* 2008; **113**(B3): B03202.
25. Marketos G, Bolton MD. Compaction bands simulated in discrete element models. *Journal of Structural Geology* 2009; **31**:479–490.
26. Roscoe KH. Tenth rankine lecture: the influence of strains in soil mechanics. *Geotechnique* 1970; **20**:129–170.
27. Mühlhaus HB, Vardoulakis I. The thickness of shear bands in granular materials. *Geotechnique* 1987; **37**:271–283.

28. Ciantia MO, Hueckel T. Weathering of submerged stressed calcarenites: chemo-mechanical coupling mechanisms. In press, *Géotechnique*, 2013.

29. Potyondy DO, Cundall PA. A bonded particle model for rock. *International Journal of Rock Mechanics and Mining Science* 2004; **41**:1329–1364.

30. Thornton C. Numerical simulations of deviatoric shear deformation of granular media. *Geotechnique* 2000; **50**(1):43–53.

31. Utili S, Nova R. DEM analysis of bonded granular geomaterials. *International Journal for Numerical and Analytical Methods in Geomechanics* 2008; **32**(17):1997–2031.

32. Utili S, Crosta GB. Modelling the evolution of natural slopes subject to weathering: Part I. Limit analysis approach. *Journal of Geophysical Research - Earth Surface* 2011a; **116**:F01016.

33. Utili S, Crosta GB. Modelling the evolution of natural slopes subject to weathering: Part II. Discrete element approach. *Journal of Geophysical Research - Earth Surface* 2011b; **116**:F01017.

34. Itasca Consulting Group, Inc. PFC3D: Particle Flow Code in 3 Dimension, Version 4.0. Itasca consulting Group Inc., Minneapolis, USA, 2008.

35. Cundall PA. Distinct element models of rock and soil structure. In Analytical and Computational Methods in Engineering Rock Mechanics, Brown T (ed.). Allen & Unwin: London, 1987; 129–163.

36. Potyondy DO. Simulating stress corrosion with a bonded-particle model for rock. *International Journal of Rock Mechanics and Mining Sciences* 2007; **44**(5):677–691.

37. Rudinick J.W., Riece J.R. Conditions for the localization of deformation in pressure-sensitive dilatants materials. *Journal of Mechanics Physics Solids* 1975; **23**:371–394.

38. Lemaitre J, Chaboche JL. Mècanique des Matèriaux Solides. Duond-Bordas: Paris, 1985.

39. Neal BG. The effect of shear and normal forces on the fully plastic moment of a beam of rectangular cross section. *Journal of Applied Mechanics* 1961; **28**:269–274.

40. Koyama T, Jing L. Effects of model scale and particle size on micro-mechanical properties and failure processes of rocks – a particle mechanics approach. *Engineering Analysis with Boundary Elements* 2007; **31**:458–472.

41. Jiang MJ, Konrad JM, Leroueil S. An efficient technique for generating homogeneous specimens for DEM studies. *Computers and geotechnics* 2005; **30**:579–597.

42. O'Sullivan C, Bray JD, Li S. A new approach for calculating strain for particulate media. *International Journal for Numerical and Analytical Methods in Geomechanics* 2003; **27**:859–877.

43. Liu WK, Li S, Belytschko T. Moving least square kernel Galerkin method.1: methodology and convergence. *Computer Methods in Applied Mechanics and Engineering* 1997; **143**:113–154.

44. Jiang MJ, Yan HB, Zhu HH, Utili S. Modelling shear behaviour and strain localisation in cemented sands by two dimensional distinct element method analyses. *Computers and Geotechnics* 2011; **38**(1):14–29.

45. Radjai F, Dubois F (eds.), Discrete Numerical Modeling of Granular Materials. vol. ISBN: 978-1-84821-260-2 (Wiley-ISTE, 2011).

46. Rudnicki JW. Conditions for compaction and shear bands in a transversally isotropic material. *International Journal of Solid and Structures* 2002; **39**:3741–3756.

47. Issen KA, Rudnicki JW. Conditions for compaction bands in porous rock. *Jounal of Geophysical Research* 2000; **105**:21529–2153.

48. Issen KA, Rudnicki JW. Theory of compaction bands in porous rock. *Physics and Chemistry of the Earth* 2001; **26**(1–2):95–100.

49. Bésuelle P. Compacting and dilating shear bands in porous rock: theoretical and experimental conditions. *Journal of Geophysical research – Solid Earth* 2000; **106**(B7):13435–13442.

50. Nova R, Castellanza R, Tamagnini C. A constitutive model for bonded geomaterials subject to mechanical and/or chemical degradation. *International Journal for Numerical and Analytical Methods in Geomechanics* 2003; **27**:705–732.